Journal of Computational Physics 539 (2025) 114209

Contents lists available at ScienceDirect

Journal of Computational Physics

journal homepage: www.elsevier.com/locate/jcp

A decoupled, linear, unconditionally stable, and fully discrete finite element scheme for two-phase ferrofluid flows with different densities and viscosities

Xiaoyong Chen [a], Rui Li [b,*], Jian Li [a,*], Xiaoming He [c]

[a] School of Electrical and Control Engineering, School of Mathematics and Data Science, Shaanxi University of Science and Technology, Xi'an, 710021, Shaanxi, China
[b] School of Mathematics and Statistics, Shaanxi Normal University, Xi'an, 710062, Shaanxi, China
[c] Department of Mathematics and Statistics, Missouri University of Science & Technology, Rolla, MO, 65409, USA

ARTICLE INFO

Keywords:
Two-phase ferrohydrodynamics
Phase field
Artificial compressibility
Different densities
Different viscosities

ABSTRACT

In this paper, a model describing the behavior of two-phase ferrofluid flows with different densities and viscosities is established by using phase field techniques. This model is a coupled nonlinear multiphysics PDE system consisting of Cahn-Hilliard equations, Navier-Stokes equations, magnetization equation and magnetostatic equation. By reformulating the magnetic potential equation, applying the artificial compressibility method, utilizing the implicit-explicit scheme for treating the nonlinear terms, and adding several stabilization terms, we propose a linear, decoupled and fully discrete finite element method approximation for the established model. And it is strictly proved to be unconditionally stable and uniquely solvable at each time step. Furthermore, the proposed scheme does not impose any artificial boundary conditions on the pressure. In order to accurately capture the diffuse interface in the numerical simulation, we also apply the adaptive mesh strategy to locally refine the mesh around the interfacial region. Several informative numerical experiments, including an accuracy test, deformation of a ferrofluid droplet, one or two air bubbles rising in ferrofluids, a controllable ferrofluid droplet in a Y-shape domain, and the Rosensweig instability under uniformly or nonuniformly applied magnetic field, are performed to illustrate various features of the proposed model and scheme, especially their applicability for the cases of high density ratio and high viscosity ratio.

1. Introduction

Ferrofluids, also called magnetic fluids, are colloidal solutions made of ferromagnetic nanoparticles suspended in a dispersing liquid. These particles are suspended by Brownian motion and do not precipitate or agglomerate under normal circumstances. Ferromagnetic fluids have the characteristics of both liquid flow and solid magnetism. Ferrofluids can be controlled by applying a magnetic field, which is very unique among all fluids. It is well known that the Rosensweig model [1–7] and the Shliomis model [8–10] are two widely accepted ferrohydrodynamics (FHD) models. Moreover, both the Rosensweig and Shliomis models deal with single-phase flows, which is the case for many technological applications, such as instrumentation, nanotechnologies, vacuum technology, enhanced heat transfer of electronics and acoustics, and so on [11–15].

However, some applications appear in the form of a two-phase flow: one of the two phases has magnetic properties and the other does not, such as magnetic manipulation of microchannel flows, microvalves, magnetically guided transport, dichroism and

* Corresponding authors.
E-mail addresses: xychen816816@163.com (X. Chen), liruismis@snnu.edu.cn (R. Li), jianli@sust.edu.cn (J. Li), hex@mst.edu (X. He).

https://doi.org/10.1016/j.jcp.2025.114209
Received 6 June 2024; Received in revised form 18 May 2025; Accepted 30 June 2025
Available online 2 July 2025

birefringence based on magneto-optic effect, biomedical engineering, location-specific drug delivery, cell separation, tagging, treatment of tumor cells, particle imaging, etc. [16–20]. Traditionally, most of the existing models for multiphase incompressible FHD problem are devoted to sharp interface models, such as the volume-of-fluid method [21–23], the level-set method [24–27], and the coupled volume-of-fluid and level-set method [28].

Recently, the lattice Boltzmann methods were developed for studying the two-phase FHD flows. In [29], Y. He and his collaborators extended the Boltzmann method of the phase field lattice to simulate the flow of multiphase ferrofluids. They proposed multiple conservative phase-field lattice Boltzmann models, which are applicable to thermal capillary flows with large density ratios and thermal physical parameters [30]. In [31], a fractional step magnetic field coupling Boltzmann model is proposed to simulate complex interfacial behaviors in magnetic multiphase flows with severe interface deformation and large density ratio, which can be recovered to the corresponding macroscopic governing equations with fully second-order accuracy. In [32], X.Y. Niu et al. presented a method combining simplified lattice Boltzmann method and self-correcting techniques to investigate the motion, deformation, and clustering of ferrofluid droplets suspended in non-magnetic fluids under different magnetic field intensities. There are also other lattice Boltzmann type works for the two-phase ferrofluid flows [33–36].

In recent years, there are also a few works focusing on macro-level phase field models with the magnetization equation for the two-phase ferrofluid flows. In [37], R. H. Nochetto et al. proposed a diffuse interface model for two-phase ferrofluid flows. Under reasonable assumptions, some nonlinear terms were dropped for simplicity. And a nonlinear fully coupled finite element method was proposed and analyzed. In [38], by combining the projection method for the Navier-Stokes equations, some subtle implicit-explicit treatments for coupled nonlinear terms, and several stabilizers, G. D. Zhang and his collaborators firstly proposed the decoupled, linear, and unconditionally energy stable scheme to solve a more complex phase field model of two-phase ferrofluid flows. In [39], the authors reformed the magnetostatic equation, introduced a scalar variable based on the "zero-energy-contribution" property, utilized the invariant energy quadratization method for the Cahn-Hilliard equations, and applied the projection method for the Navier-Stokes model, in order to construct the first linear, full decoupled scheme, second order in time accuracy and unconditionally energy stable for the two-phase FHD model. In [40], the authors introduced a two-phase ferrofluid flow model of Allen-Cahn type that conserved mass and developed a unified framework of the scalar auxiliary variable (SAV) method and the zero energy contribution (ZEC) approach. The models and finite element methods in [37–40] are proposed for two-phase ferrofluid flows of matched density and use strict pressure boundary treatment.

In this paper, we extend the model in [37] by considering the case of nonmatching density. The main goal of this paper is to develop a linear, decoupled, unconditionally stable, and fully discrete numerical scheme to approximate the solution of this model. Even with the existing works, significant challenges still remain in the development and analysis of the numerical method, due to a series of strong nonlinear couplings among the pressure, velocity, magnetization field, phase variable, and effective magnetization field through the nontrivial elastic stress tensor, fluid convection, and Kelvin force. The main difficulty in achieving this goal is how to linearize the coupled nonlinear term and decouple the velocity and pressure, while maintaining the unconditional stability.

Two-phase ferrofluid model with different densities and viscosities consists of Cahn-Hilliard equations, Navier-Stokes equations, magnetization equation, and magnetostatic equation. For the Cahn-Hilliard equations, there exist a series of successful techniques to discretize the nonlinear potential to obtain energy stable schemes, such as the convex splitting method [41–45], the stabilize explicit method [46–49], the invariant energy quadratization method [50–56], the scalar auxiliary variable method [57–62], the zero-energy-contribution method [63–68], and so on. For the Navier-Stokes equations, there are also a series of successful decoupling techniques, such as the projection method [69–73] and the artificial compressibility method [74–76]. The main difference between these two methods is whether one needs to impose any artificial boundary conditions on the pressure.

To design the target numerical method, we reformulate the magnetostatic equation, employ the artificial compressibility method for decoupling the velocity and pressure in the Navier-Stokes equation, utilize the implicit-explicit techique for handling the coupled nonlinear term, and add several first-order stability terms. As a result, we propose a linear, decoupled, fully discrete finite element numerical scheme to solve the two-phase FHD systems with different densities and viscosities. The proposed scheme is unconditionally stable and uniquely solvable at each time step. It also does not enforce any artificial boundary condition on the pressure. Furthermore, we introduce the adaptive grid strategy to dramatically accelerate the computation without sacrificing the desired properties and accuracy. In the numerical experiments, we use the proposed numerical scheme to simulate some practical problems and obtain physically meaningful results, including deformation of a ferrofluid droplet, one or two air bubbles rising in ferrofluids, a controllable ferrofluid droplet in a Y-shape domain, and the Rosensweig instability under uniformly or nonuniformly applied magnetic field. This is by no means an easy task due to the cases of high density ratio and high viscosity ratio.

The rest of this paper is organized as follows. In Section 2, a two-phase ferrofluid model with different densities and viscosities is presented. With the help of a new variable, we obtain an equivalent form of this model and derive its energy law. In Section 3, we derive the weak formulation and semi-discrrete formulations for the proposed model. In Section 4, we propose the numerical scheme, and strictly prove its unconditional energy stability and uniquely solvability at each time step. In Section 5, a series of numerical experiments are provided to illustrate the features of the proposed model and scheme. Then the conclusions are drawn in the Section 6.

2. A two-phase ferrofluid model with different densities and viscosities

In this section, we extend the two-phase FHD model in [37] by considering the case of nonmatching density. Then an equivalent form of this model is derived by introducing a new variable. The dissipative energy law is also showed at the continuous level.

2.1. Model system

Under the linear assumption $\boldsymbol{m} \approx \chi \boldsymbol{h}$ [23], the terms $\frac{\mu}{2}\nabla \times (\boldsymbol{m} \times \boldsymbol{h})$ and $\beta \boldsymbol{m} \times (\boldsymbol{m} \times \boldsymbol{h})$ are negligible. Under the assumption that convection and reaction are the domain terms, the term $-\frac{1}{2}\nabla \times \boldsymbol{u} \times \boldsymbol{m}$ of the magnetization equation is negligible [37]. As a result, the following matched density two-phase FHD model [37] was proposed in a polygonal domain Ω:

$$\Phi_t + \nabla \cdot (\boldsymbol{u}\Phi) = M\Delta W, \tag{1a}$$

$$W = -\varepsilon \Delta \Phi + f(\Phi), \tag{1b}$$

$$\rho(\boldsymbol{u}_t + (\boldsymbol{u} \cdot \nabla)\boldsymbol{u}) - \nabla \cdot (\nu(\Phi) D(\boldsymbol{u})) + \nabla p + \frac{\lambda}{\varepsilon}\Phi \nabla W = \mu(\boldsymbol{m} \cdot \nabla)\boldsymbol{h}, \tag{1c}$$

$$\nabla \cdot \boldsymbol{u} = 0, \tag{1d}$$

$$\boldsymbol{m}_t + (\boldsymbol{u} \cdot \nabla)\boldsymbol{m} = -\frac{1}{\tau}(\boldsymbol{m} - \chi(\Phi)\boldsymbol{h}), \tag{1e}$$

$$-\Delta \varphi = \nabla \cdot (\boldsymbol{m} - \boldsymbol{h}_a). \tag{1f}$$

Here Φ is the phase field variable, W is the chemical potential, $0 < \varepsilon \ll 1$ is related to the interface thickness, $M > 0$ is the mobility parameter, $\boldsymbol{u}$ is the velocity field, p is the pressure, $\nu(\Phi)$ is the dynamic viscosity, λ is the capillary coefficient, μ is the permeability of free space, $\boldsymbol{m}$ is the magnetization field, $\boldsymbol{h}(:= \nabla\varphi)$ is the effective magnetizing field, φ is the magnetic potential, $\boldsymbol{h} = \boldsymbol{h}_a + \boldsymbol{h}_d$ where $\boldsymbol{h}_a$ is the given applied magnetizing field satisfying curl-free and div-free conditions, $\boldsymbol{h}_d$ is the so-called demagnetizing field, $\chi(\Phi)$ is the susceptibility, τ is relaxation time constant, $D(\boldsymbol{u}) = \frac{1}{2}(\nabla \boldsymbol{u} + (\nabla \boldsymbol{u})^{\mathrm{t}})$, and the term $(\boldsymbol{m} \cdot \nabla)\boldsymbol{h}$ is the so-called Kelvin force. Moreover, $f(\Phi) = F'(\Phi)$, where $F(\Phi)$ is a given double well potential as follows:

$$F(\Phi) = \begin{cases} \frac{1}{4\varepsilon}\Phi^2, & \Phi \in (-\infty, 0), \\ \frac{1}{4\varepsilon}\Phi^2(\Phi - 1)^2, & \Phi \in [0, 1], \\ \frac{1}{4\varepsilon}(\Phi - 1)^2, & \Phi \in (1, +\infty). \end{cases} \tag{2}$$

It is easy to check that the second derivative of the double well potential $F(\Phi)$ is bounded, that is, $|F''(\Phi)| \le \frac{1}{2\varepsilon}$. The phase field variable Φ satisfies

$$\Phi(t, \boldsymbol{x}) = \begin{cases} 1, & \text{ferrofluid phase}, \\ 0, & \text{nonmagnetizable viscous medium}. \end{cases} \tag{3}$$

Without loss of generality, we can take density $\rho = 1$ in (1c). In this work we extend the model (2.1) by considering the case of nonmatching density for which the density ρ is not a constant but a function related to the phase field variable Φ. Inspired by [77,78], we know that the momentum Eq. (1c) can be rewritten as

$$\rho(\Phi)(\boldsymbol{u}_t + (\boldsymbol{u} \cdot \nabla)\boldsymbol{u}) - \nabla \cdot (\nu(\Phi) D(\boldsymbol{u})) + \nabla p + \frac{\lambda}{\varepsilon}\Phi \nabla W = \mu(\boldsymbol{m} \cdot \nabla)\boldsymbol{h}. \tag{4}$$

Therefore, replacing (1c) in model (2.1) with (4), we obtain the following model with different densities and viscosities in Ω:

$$\Phi_t + \nabla \cdot (\boldsymbol{u}\Phi) = M\Delta W, \tag{5a}$$

$$W = -\varepsilon \Delta \Phi + f(\Phi), \tag{5b}$$

$$\rho(\Phi)(\boldsymbol{u}_t + (\boldsymbol{u} \cdot \nabla)\boldsymbol{u}) - \nabla \cdot (\nu(\Phi) D(\boldsymbol{u})) + \nabla p + \frac{\lambda}{\varepsilon}\Phi \nabla W = \mu(\boldsymbol{m} \cdot \nabla)\boldsymbol{h}, \tag{5c}$$

$$\nabla \cdot \boldsymbol{u} = 0, \tag{5d}$$

$$\boldsymbol{m}_t + (\boldsymbol{u} \cdot \nabla)\boldsymbol{m} = -\frac{1}{\tau}(\boldsymbol{m} - \chi(\Phi)\boldsymbol{h}), \tag{5e}$$

$$-\Delta \varphi = \nabla \cdot (\boldsymbol{m} - \boldsymbol{h}_a), \tag{5f}$$

for every $t \in (0, T]$, where $\rho(\Phi)$, $\nu(\Phi)$ and $\chi(\Phi)$ are density, viscosity and susceptibility depending on the phase-field variable Φ and satisfying

$$0 < \min\{\rho_w, \rho_f\} \le \rho(\Phi) \le \max\{\rho_w, \rho_f\},\ 0 < \min\{\nu_w, \nu_f\} \le \nu(\Phi) \le \max\{\nu_w, \nu_f\},\ 0 \le \chi(\Phi) \le \chi_0(\Phi). \tag{6}$$

Here $\chi_0(\Phi) > 0$ is the magnetic susceptibility of the ferrofluid phase, ν_w and ρ_w are the viscosity and density of the non-magnetic phase, ν_f and ρ_f are the viscosity and density of the ferrofluid, respectively.

For the two-phase FHD model (2.5) with different densities and viscosities, the main goal of this paper is to develop a decoupled, linear, unconditionally stable, and fully discrete numerical scheme to approximate the solution. It is well known that the skew-symmetric property is one of the important properties of the nonlinear term for the incompressible Navier-Stokes equations with constant density and certain boundary conditions. That is, since $\nabla \cdot \boldsymbol{u} = 0$ and $\boldsymbol{u}|_{\partial\Omega} = \boldsymbol{0}$, one has

$$\int_\Omega \rho_0(\boldsymbol{u} \cdot \nabla)\boldsymbol{v} \cdot \boldsymbol{v} \mathrm{d}\boldsymbol{x} = 0. \tag{7}$$

However, if the constant ρ_0 above is replaced by the non-constant function ρ related to the phase field variable Φ, then (7) is not valid. To overcome this difficulty, we follow [78,79] to introduce a new variable $\sigma = \sqrt{\rho(\Phi)}$ to derive the equivalent form of system (2.5). Using the mass conservation

$$\rho_t(\Phi) + \nabla \cdot (\rho(\Phi)\boldsymbol{u}) = 0, \tag{8}$$

we derive

$$\sigma(\sigma\boldsymbol{u})_t = \rho(\Phi)\boldsymbol{u}_t + \frac{1}{2}\rho_t(\Phi)\boldsymbol{u} = \rho(\Phi)\boldsymbol{u}_t - \frac{1}{2}\nabla \cdot (\rho(\Phi)\boldsymbol{u})\boldsymbol{u}, \tag{9}$$

then

$$\rho(\Phi)\boldsymbol{u}_t = \sigma(\sigma\boldsymbol{u})_t + \frac{1}{2}\nabla \cdot (\rho(\Phi)\boldsymbol{u})\boldsymbol{u}, \tag{10}$$

thus it is physically consistent to replace $\rho(\Phi)\boldsymbol{u}_t$ in (5c) by $\sigma(\sigma\boldsymbol{u})_t + \frac{1}{2}\nabla \cdot (\rho(\Phi)\boldsymbol{u})\boldsymbol{u}$, leading to the modified momentum equation

$$\sigma(\sigma\boldsymbol{u})_t + \frac{1}{2}\nabla \cdot (\rho(\Phi)\boldsymbol{u})\boldsymbol{u} + (\rho(\Phi)\boldsymbol{u} \cdot \nabla)\boldsymbol{u} - \nabla \cdot (\nu(\Phi)D(\boldsymbol{u})) + \nabla p + \frac{\lambda}{\varepsilon}\Phi\nabla W = \mu(\boldsymbol{m} \cdot \nabla)\boldsymbol{h}. \tag{11}$$

Since $\boldsymbol{u} \cdot \boldsymbol{n}|_{\partial\Omega} = 0$, we obtain

$$((\rho(\Phi)\boldsymbol{u} \cdot \nabla)\boldsymbol{v}, \boldsymbol{v}) + \frac{1}{2}(\nabla \cdot (\rho(\Phi)\boldsymbol{u})\boldsymbol{v}, \boldsymbol{v}) = 0. \tag{12}$$

Therefore, the equivalent form of two-phase ferrofluid with different densities and viscosities can be obtained as follows:

$$\Phi_t + \nabla \cdot (\boldsymbol{u}\Phi) = M\Delta W, \tag{13a}$$

$$W = -\varepsilon\Delta\Phi + f(\Phi), \tag{13b}$$

$$\sigma(\sigma\boldsymbol{u})_t + \frac{1}{2}\nabla \cdot (\rho(\Phi)\boldsymbol{u})\boldsymbol{u} + (\rho(\Phi)\boldsymbol{u} \cdot \nabla)\boldsymbol{u} - \nabla \cdot (\nu(\Phi)D(\boldsymbol{u})) + \nabla p + \frac{\lambda}{\varepsilon}\Phi\nabla W = \mu(\boldsymbol{m} \cdot \nabla)\boldsymbol{h}, \tag{13c}$$

$$\nabla \cdot \boldsymbol{u} = 0, \tag{13d}$$

$$\boldsymbol{m}_t + (\boldsymbol{u} \cdot \nabla)\boldsymbol{m} = -\frac{1}{\tau}(\boldsymbol{m} - \chi(\Phi)\boldsymbol{h}), \tag{13e}$$

$$-\Delta\varphi = \nabla \cdot (\boldsymbol{m} - \boldsymbol{h}_a). \tag{13f}$$

We supplement system (13a)–(13f) with the following initial and boundary conditions

$$\Phi(0, \boldsymbol{x}) = \Phi_0,\ \boldsymbol{u}(0, \boldsymbol{x}) = \boldsymbol{u}_0,\ \boldsymbol{m}(0, \boldsymbol{x}) = \boldsymbol{m}_0, \tag{14a}$$

$$\partial_n\Phi|_{\partial\Omega} = 0,\ \partial_n W|_{\partial\Omega} = 0,\ \boldsymbol{u}|_{\partial\Omega} = \boldsymbol{0},\ \partial_n\varphi|_{\partial\Omega} = (\boldsymbol{h}_a - \boldsymbol{m}) \cdot \boldsymbol{n}, \tag{14b}$$

where $\boldsymbol{n}$ is the outward normal on the boundary $\partial\Omega$. Moreover, under the condition of satisfying inequalities (6) [38,80,81], we select

$$\rho(\Phi) = (\rho_f - \rho_w)\Phi + \rho_w,\ \nu(\Phi) = (\nu_f - \nu_w)\Phi + \nu_w,\ \chi(\Phi) = \chi_0\Phi. \tag{15}$$

2.2. The dissipative energy law

For the convenience of mathematical deduction, we first introduce some notations in this paper. We use $\|\cdot\|_{s,p}$ to denote the standard norm of the Sobolev space $W^{s,p}(\Omega)$. When $p = 2$, we use $\|\cdot\|_{H^1}$ to denote the norm of $W^{1,2}(\Omega) = H^1(\Omega)$. In particular, $s = 0$, $W^{0,p} = L^p(\Omega)$. The inner product in $L^2(\Omega)$ is associated with $(\cdot, \cdot)$ and the norm of $L^2(\Omega)$ is denoted by $\|\cdot\|$. Moreover, we define a trilinear form as $b(\boldsymbol{m}, \boldsymbol{h}, \boldsymbol{u}) = ((\boldsymbol{m} \cdot \nabla)\boldsymbol{h}, \boldsymbol{u})$. Thus, we recall an important lemma to derive the energy estimate as follows:

Lemma 2.1 ([37]). *Let $\boldsymbol{m}$ be the magnetization, $\boldsymbol{h}$ be the effective magnetizing field, $\boldsymbol{u}$ be a solenoidal field such that $\boldsymbol{u} \cdot \boldsymbol{n} = 0$ on $\partial\Omega$. Then the following identity holds true*

$$b(\boldsymbol{u}, \boldsymbol{m}, \boldsymbol{h}) = -b(\boldsymbol{m}, \boldsymbol{h}, \boldsymbol{u}). \tag{16}$$

Theorem 2.1. *The two-phase ferrofluid system (2.13) with different densities and viscosities satisfies the following energy law:*

$$\begin{aligned}&\frac{\mathrm{d}}{\mathrm{d}t}\left(\frac{\lambda}{2}\|\nabla\Phi\|^2 + \frac{\lambda}{\varepsilon}(F(\Phi), 1) + \frac{1}{2}\|\sigma\boldsymbol{u}\|^2 + \frac{\mu}{2\chi_0}\|\boldsymbol{m}\|^2 + \frac{\mu}{2}\|\boldsymbol{h}\|^2\right) + \frac{\lambda M}{\varepsilon}\|\nabla W\|^2 \\ &\quad + \|\sqrt{\nu(\Phi)}D(\boldsymbol{u})\|^2 + \frac{3\mu}{4\tau\chi_0}\|\boldsymbol{m}\|^2 \le \frac{\mu}{2\tau}\|\boldsymbol{h}_a\|^2 + \frac{\tau\mu}{2}\|(\boldsymbol{h}_a)_t\|^2.\end{aligned} \tag{17}$$

Proof. Multiplying (13a) by $\frac{\lambda}{\varepsilon}W$ and (13b) by $\frac{\lambda}{\varepsilon}\Phi_t$, respectively, and using integration by parts, we obtain

$$\frac{\lambda}{\varepsilon}(\Phi_t, W) + \frac{\lambda M}{\varepsilon}\|\nabla W\|^2 = \frac{\lambda}{\varepsilon}(\boldsymbol{u}\Phi, \nabla W), \tag{18}$$

$$\frac{\lambda}{\varepsilon}(W, \Phi_t) = \frac{\mathrm{d}}{\mathrm{d}t}\left(\frac{\lambda}{2}\|\nabla\Phi\|^2 + \frac{\lambda}{\varepsilon}(F(\Phi), 1)\right). \tag{19}$$

By taking the L^2 inner product of (13c) with $\boldsymbol{u}$, applying integration by parts, and using Lemma 2.1 for the Kelvin force, (12) and (13d), we derive

$$\frac{1}{2}\frac{\mathrm{d}}{\mathrm{d}t}\|\sigma\boldsymbol{u}\|^2 + \|\sqrt{\nu(\Phi)}D(\boldsymbol{u})\|^2 + \frac{\lambda}{\varepsilon}(\Phi\nabla W, \boldsymbol{u}) = -\mu b(\boldsymbol{u}, \boldsymbol{m}, \boldsymbol{h}). \tag{20}$$

Multiplying (13e) by $-\mu\boldsymbol{h}$ and $\frac{\mu}{\chi_0}\boldsymbol{m}$, respectively, yield

$$-\mu(\boldsymbol{m}_t, \boldsymbol{h}) - \frac{\mu}{\tau}(\boldsymbol{m}, \boldsymbol{h}) + \frac{\mu}{\tau}\|\sqrt{\chi(\Phi)}\boldsymbol{h}\|^2 = \mu b(\boldsymbol{u}, \boldsymbol{m}, \boldsymbol{h}), \tag{21}$$

$$\frac{\mu}{2\chi_0}\frac{\mathrm{d}}{\mathrm{d}t}\|\boldsymbol{m}\|^2 + \frac{\mu}{\tau\chi_0}\|\boldsymbol{m}\|^2 = \frac{\mu}{\tau\chi_0}(\chi(\Phi)\boldsymbol{h}, \boldsymbol{m}), \tag{22}$$

where we use $((\boldsymbol{u}\cdot\nabla)\boldsymbol{m}, \boldsymbol{m}) = ((\boldsymbol{u}\cdot\nabla)\boldsymbol{m}, \boldsymbol{m}) + \frac{1}{2}((\nabla\cdot\boldsymbol{u})\boldsymbol{m}, \boldsymbol{m}) = 0$. By taking the L^2 inner product of (13f) with $\frac{\mu}{\tau}\varphi$, and using $\boldsymbol{h} = \nabla\varphi$, we derive

$$\frac{\mu}{\tau}\|\boldsymbol{h}\|^2 + \frac{\mu}{\tau}(\boldsymbol{m}, \boldsymbol{h}) = \frac{\mu}{\tau}(\boldsymbol{h}_a, \boldsymbol{h}). \tag{23}$$

By taking the time derivative of (13f), multiplying the resulted equation by $\mu\varphi$, and using integration by parts and $\boldsymbol{h} = \nabla\varphi$, we obtain

$$\frac{\mu}{2}\frac{\mathrm{d}}{\mathrm{d}t}\|\boldsymbol{h}\|^2 + \mu(\boldsymbol{m}_t, \boldsymbol{h}) = \mu((\boldsymbol{h}_a)_t, \boldsymbol{h}). \tag{24}$$

Thus, summing up (18)–(24), and applying Lemma 2.1, we derive

$$\begin{aligned}&\frac{\mathrm{d}}{\mathrm{d}t}\left(\frac{\lambda}{2}\|\nabla\Phi\|^2 + \frac{\lambda}{\varepsilon}(F(\Phi), 1) + \frac{1}{2}\|\sigma\boldsymbol{u}\|^2 + \frac{\mu}{2\chi_0}\|\boldsymbol{m}\|^2 + \frac{\mu}{2}\|\boldsymbol{h}\|^2\right) + \frac{\lambda M}{\varepsilon}\|\nabla W\|^2 + \|\sqrt{\nu(\Phi)}D(\boldsymbol{u})\|^2\\ &\quad + \frac{\mu}{\tau}\|\boldsymbol{h}\|^2 + \frac{\mu}{\tau\chi_0}\|\boldsymbol{m}\|^2 + \frac{\mu}{\tau}\|\sqrt{\chi(\Phi)}\boldsymbol{h}\|^2 = \frac{\mu}{\tau\chi_0}(\chi(\Phi)\boldsymbol{h}, \boldsymbol{m}) + \frac{\mu}{\tau}(\boldsymbol{h}_a, \boldsymbol{h}) + \mu((\boldsymbol{h}_a)_t, \boldsymbol{h}).\end{aligned} \tag{25}$$

The three terms to the right of (25) can be estimated as

$$\begin{aligned}&\frac{\mu}{\tau\chi_0}(\chi(\Phi)\boldsymbol{h}, \boldsymbol{m}) + \frac{\mu}{\tau}(\boldsymbol{h}_a, \boldsymbol{h}) + \mu((\boldsymbol{h}_a)_t, \boldsymbol{h})\\ &\le \frac{\mu}{\tau}\|\sqrt{\chi(\Phi)}\boldsymbol{h}\|^2 + \frac{\mu\chi(\Phi)}{4\tau\chi_0^2}\|\boldsymbol{m}\|^2 + \frac{\mu}{\tau}\|\boldsymbol{h}\|^2 + \frac{\mu}{2\tau}\|\boldsymbol{h}_a\|^2 + \frac{\tau\mu}{2}\|(\boldsymbol{h}_a)_t\|^2\\ &\le \frac{\mu}{\tau}\|\sqrt{\chi(\Phi)}\boldsymbol{h}\|^2 + \frac{\mu}{4\tau\chi_0}\|\boldsymbol{m}\|^2 + \frac{\mu}{\tau}\|\boldsymbol{h}\|^2 + \frac{\mu}{2\tau}\|\boldsymbol{h}_a\|^2 + \frac{\tau\mu}{2}\|(\boldsymbol{h}_a)_t\|^2.\end{aligned} \tag{26}$$

Here $\boldsymbol{h}_a$ is a given external magnetic field serving as a source term and may change over time. Thus the system (2.13) satisfies energy law (17). □

3. The weak formulation and semi-discrete formulation for two-phase FHD model with different densities and viscosities

For the mathematical setting of problem (2.13), a series of spaces are introduced as follows:

$$\begin{cases} Y = H^1(\Omega) = \{\phi \in H^1(\Omega)\},\\ \boldsymbol{V} = \boldsymbol{H_0^1}(\Omega) = \{\boldsymbol{v} \in \boldsymbol{H^1}(\Omega) : \boldsymbol{v} = \boldsymbol{0} \text{ on } \partial\Omega\},\\ Q = L_0^2(\Omega) = \{q \in L^2(\Omega) : \int_\Omega q\,\mathrm{d}\boldsymbol{x} = 0\},\\ \boldsymbol{N} = \boldsymbol{L^2}(\Omega) = \{\boldsymbol{c} \in \boldsymbol{L^2}(\Omega)\},\\ Z = H^1(\Omega) = \{\psi \in H^1(\Omega) \cap L_0^2(\Omega)\}. \end{cases} \tag{27}$$

We then derive the weak formulation of two-phase FHD model (2.13). We firstly consider the magnetic potential Eq. (13f): find $\varphi \in Z$, such that

$$\frac{1}{\tau}(\nabla\varphi, \nabla\psi) + \frac{1}{\tau}(\boldsymbol{m}, \nabla\psi) = \frac{1}{\tau}(\boldsymbol{h}_a, \nabla\psi),\ \forall\psi \in Z. \tag{28}$$

By taking the temporal derivative of (13f) and formulating the obtained equation in the weak formulation, we obtain

$$(\nabla\varphi_t, \nabla\psi) + (\boldsymbol{m}_t, \nabla\psi) = ((\boldsymbol{h}_a)_t, \nabla\psi). \tag{29}$$

Summing up (28) and (29), we obtain the following new magnetostatic equation which will be used to replace (13f):

$$\frac{1}{\tau}(\nabla\varphi, \nabla\psi) + (\nabla\varphi_t, \nabla\psi) + \frac{1}{\tau}(\boldsymbol{m}, \nabla\psi) + (\boldsymbol{m}_t, \nabla\psi) = \frac{1}{\tau}(\boldsymbol{h}_a, \nabla\psi) + ((\boldsymbol{h}_a)_t, \nabla\psi). \tag{30}$$

Remark 3.1. *It is well known that the analysis of the discrete energy law of a numerical scheme usually follows the same route as that of the energy law of the PDE system. Hence it is expected that two test functions are needed to be taken for (13e) and (13f) from the proof of Theorem 2.1. Inspiring by [39], we construct a new magnetostatic Eq. (30) to avoid taking two test functions in (13f). See Remark 4.3 for more details about addressing the problem of taking two test functions in (13e).*

Then we obtain the weak formulation of the two-phase FHD model (2.13) with different densities and viscosities: find $(\Phi, W, \boldsymbol{u}, p, \boldsymbol{m}, \varphi) \in Y \times Y \times \boldsymbol{V} \times Q \times \boldsymbol{N} \times Z$ such that $(\phi, w, \boldsymbol{v}, q, \boldsymbol{c}, \psi) \in Y \times Y \times \boldsymbol{V} \times Q \times \boldsymbol{N} \times Z$,

$$\begin{cases} (\Phi_t, \phi) - (\boldsymbol{u}\Phi, \nabla\phi) = -M(\nabla W, \nabla\phi), \\ (W, w) = \varepsilon(\nabla\Phi, \nabla w) + (f(\Phi), w), \\ (\sigma(\sigma\boldsymbol{u})_t, \boldsymbol{v}) + B(\rho(\Phi)\boldsymbol{u}, \boldsymbol{u}, \boldsymbol{v}) + (\nu(\Phi)D(\boldsymbol{u}), D(\boldsymbol{v})) - (p, \nabla\cdot\boldsymbol{v}) + \frac{\lambda}{\varepsilon}(\Phi\nabla W, \boldsymbol{v}) = \mu((\boldsymbol{m}\cdot\nabla)\boldsymbol{h}, \boldsymbol{v}), \\ (\nabla\cdot\boldsymbol{u}, q) = 0, \\ (\boldsymbol{m}_t, \boldsymbol{c}) + ((\boldsymbol{u}\cdot\nabla)\boldsymbol{m}, \boldsymbol{c}) = -\frac{1}{\tau}(\boldsymbol{m}, \boldsymbol{c}) + \frac{1}{\tau}(\chi(\Phi)\boldsymbol{h}, \boldsymbol{c}), \\ \frac{1}{\tau}(\nabla\varphi, \nabla\psi) + (\nabla\varphi_t, \nabla\psi) + \frac{1}{\tau}(\boldsymbol{m}, \nabla\psi) + (\boldsymbol{m}_t, \nabla\psi) = \frac{1}{\tau}(\boldsymbol{h}_a, \nabla\psi) + ((\boldsymbol{h}_a)_t, \nabla\psi), \end{cases} \tag{31}$$

where

$$B(\rho(\Phi)\boldsymbol{u}, \boldsymbol{v}, \boldsymbol{w}) = \frac{1}{2}((\rho(\Phi)\boldsymbol{u}\cdot\nabla)\boldsymbol{v}, \boldsymbol{w}) - \frac{1}{2}((\rho(\Phi)\boldsymbol{u}\cdot\nabla)\boldsymbol{w}, \boldsymbol{v}). \tag{32}$$

We set that the polygonal/polyhedral domain Ω is discretized by a conforming and shape regular triangulation/tetrahedron $\mathcal{T}_h$ that is composed by open disjoint elements K such that $\overline{\Omega} = \bigcup_{K\in\mathcal{T}_h}\overline{K}$. In order to derive the semi-discrete formulations of two-phase FHD model with different densities and viscosities, we take a series of the finite dimensional subspaces:

$$Y_h \subset Y,\ \boldsymbol{V}_h \subset \boldsymbol{V},\ Q_h \subset Q,\ \boldsymbol{N}_h \subset \boldsymbol{N},\ Z_h \subset Z, \tag{33}$$

where

$$\begin{cases} Y_h = \{\phi_h \in C^o(\Omega) : \phi_h|_K \in P_{l_1}(K),\ \forall K \in \mathcal{T}_h\}, \\ \boldsymbol{V}_h = \{\boldsymbol{v}_h \in \boldsymbol{C}^o(\Omega) : \boldsymbol{v}_h|_K \in \boldsymbol{P}_{l_2}(K),\ \forall K \in \mathcal{T}_h\}, \\ Q_h = \{q_h \in C^o(\Omega) : q_h|_K \in P_{l_2-1}(K),\ \forall K \in \mathcal{T}_h\}, \\ \boldsymbol{N}_h = \{\boldsymbol{c}_h \in \boldsymbol{C}^o(\Omega) : \boldsymbol{c}_h|_K \in \boldsymbol{P}_{l_3-1}(K),\ \forall K \in \mathcal{T}_h\}, \\ Z_h = \{\psi_h \in C^o(\Omega) : \psi_h|_K \in P_{l_3}(K),\ \forall K \in \mathcal{T}_h\}. \end{cases} \tag{34}$$

Here P_l and $\boldsymbol{P}_l$ are the scalar and vector spaces of polynomials of total degree at most l, respectively. Furthermore, we set the pair of spaces $(\boldsymbol{V}_h, Q_h)$ satisfy inf-sup compatibility condition [82] as follows:

$$\beta\|q_h\| \le \sup_{\boldsymbol{v}_h\in\boldsymbol{V}_h, \boldsymbol{v}_h\neq\boldsymbol{0}} \frac{(\nabla\cdot\boldsymbol{v}_h, q_h)}{\|\nabla\boldsymbol{v}_h\|},\ \forall q_h \in Q_h, \tag{35}$$

where the constant $\beta > 0$ only relys on Ω. Thus we obtain the semi-discrete formulation of the system (31) as follows: find $(\Phi_h, W_h, \boldsymbol{u}_h, p_h, \boldsymbol{m}_h, \varphi_h) \in Y_h \times Y_h \times \boldsymbol{V}_h \times Q_h \times \boldsymbol{N}_h \times Z_h$ such that $(\phi_h, w_h, \boldsymbol{v}_h, q_h, \boldsymbol{c}_h, \psi_h) \in Y_h \times Y_h \times \boldsymbol{V}_h \times Q_h \times \boldsymbol{N}_h \times Z_h$,

$$\begin{cases} (\Phi_{ht}, \phi_h) - (\boldsymbol{u}_h\Phi_h, \nabla\phi_h) + M(\nabla W_h, \nabla\phi_h) = 0, \\ (W_h, w_h) = \varepsilon(\nabla\Phi_h, \nabla w_h) + (f(\Phi_h), w_h), \\ (\sigma_h(\sigma\boldsymbol{u})_{ht}, \boldsymbol{v}_h) + B(\rho(\Phi_h)\boldsymbol{u}_h, \boldsymbol{u}_h, \boldsymbol{v}_h) + (\nu(\Phi_h)D(\boldsymbol{u}_h), D(\boldsymbol{v}_h)) - (p_h, \nabla\cdot\boldsymbol{v}_h) + \frac{\lambda}{\varepsilon}(\Phi_h\nabla W_h, \boldsymbol{v}_h) \\ \quad = \mu((\boldsymbol{m}_h\cdot\nabla)\boldsymbol{h}_h, \boldsymbol{v}_h), \\ (\nabla\cdot\boldsymbol{u}_h^n, q_h) = 0, \\ (\boldsymbol{m}_{ht}, \boldsymbol{c}_h) + ((\boldsymbol{u}_h\cdot\nabla)\boldsymbol{m}_h, \boldsymbol{c}_h) = -\frac{1}{\tau}(\boldsymbol{m}_h, \boldsymbol{c}_h) + \frac{1}{\tau}(\chi(\Phi_h)\boldsymbol{h}_h, \boldsymbol{c}_h), \\ \frac{1}{\tau}(\nabla\varphi_h, \nabla\psi_h) + (\nabla\varphi_{ht}, \nabla\psi_h) + \frac{1}{\tau}(\boldsymbol{m}_h, \nabla\psi_h) + (\boldsymbol{m}_{ht}, \nabla\psi_h) = \frac{1}{\tau}(\boldsymbol{h}_a, \nabla\psi_h) + ((\boldsymbol{h}_a)_t, \nabla\psi_h), \end{cases} \tag{36}$$

where $\sigma_h = \sqrt{\rho(\Phi_h)}$ and $\boldsymbol{h}_h = \nabla\varphi_h$.

Similar to the proof of Theorem 2.1, we deduce the following energy law of the semi-discrete formulation.

Theorem 3.1. *The semi-discrete formulation (36) of two-phase ferrofluid system (2.13) with different densities and viscosities satisfies the following energy law:*

$$\begin{aligned} &\frac{\mathrm{d}}{\mathrm{d}t}\left(\frac{\lambda}{2}\|\nabla\Phi_h\|^2 + \frac{\lambda}{\varepsilon}(F(\Phi_h), 1) + \frac{1}{2}\|\sigma_h\boldsymbol{u}_h\|^2 + \frac{\mu}{2\chi_0}\|\boldsymbol{m}_h\|^2 + \frac{\mu}{2}\|\boldsymbol{h}_h\|^2\right) + \frac{\lambda M}{\varepsilon}\|\nabla W_h\|^2 \\ &\quad + \|\sqrt{\nu(\Phi_h)}D(\boldsymbol{u}_h)\|^2 + \frac{3\mu}{4\tau\chi_0}\|\boldsymbol{m}_h\|^2 \le \frac{\mu}{2\tau}\|\boldsymbol{h}_a\|^2 + \frac{\tau\mu}{2}\|(\boldsymbol{h}_a)_t\|^2. \end{aligned} \tag{37}$$

4. Fully discrete scheme

In this section, we aim to develop linear, decoupled and fully discrete numerical scheme to solve the semidiscrete formulation (36) of two-phase FHD model with different densities and viscosities. This scheme is not only easy to implement for temporal discretization and spatial discretization, but also unconditionally energy stable. For this purpose, let $N > 0$ be the total number of time steps, define the uniform time step size as $dt = \frac{T}{N}$, and assume $t_n = ndt$. We also define the backward difference operator d_t as $d_t\xi^n = \frac{\xi^n - \xi^{n-1}}{dt}$ for any variable ξ. Then the numerical scheme reads as follows.

Step 0. Initially, given $\boldsymbol{m}_h^0$ and $\boldsymbol{h}_a^0$, we find $\varphi_h^0 \in Z_h$ such that for all $\psi_h \in Z_h$

$$(\nabla\varphi_h^0, \nabla\psi_h) = -(\boldsymbol{m}_h^0, \nabla\psi_h) + (\boldsymbol{h}_a^0, \nabla\psi_h). \tag{38}$$

Step 1. Find $(\Phi_h^n, W_h^n) \in Y_h \times Y_h$ such that for all $(\phi_h, \omega_h) \in Y_h \times Y_h$

$$(d_t\Phi_h^n, \phi_h) + M(\nabla W_h^n, \nabla\phi_h) + \frac{\lambda dt}{2\varepsilon}\left(\frac{1}{\sigma_h^{n-1}}\Phi_h^{n-1}\nabla W_h^n, \frac{1}{\sigma_h^{n-1}}\Phi_h^{n-1}\nabla\phi_h\right) = (\boldsymbol{u}_h^{n-1}\Phi_h^{n-1}, \nabla\phi_h), \tag{39}$$

$$(W_h^n, w_h) - \varepsilon(\nabla\Phi_h^n, \nabla w_h) = (f(\Phi_h^{n-1}), w_h) + S(\Phi_h^n - \Phi_h^{n-1}, w_h), \tag{40}$$

where $\sigma_h^{n-1} = \sqrt{\rho(\Phi_h^{n-1})}$ and $S > 0$ is the stabilization parameter.

Step 2. Set $\boldsymbol{h}_h^{n-1} = \nabla\varphi_h^{n-1}$, find $\boldsymbol{u}_h^n \in \boldsymbol{V}_h$ satisfying $\boldsymbol{u}_h^n|_{\partial\Omega} = 0$ such that for all $\boldsymbol{v}_h \in \boldsymbol{V}_h$

$$\begin{aligned}&\left(\sigma_h^{n-1}\frac{\sigma_h^{n-1}\boldsymbol{u}_h^n - \sigma_h^{n-1}\boldsymbol{u}_h^{n-1}}{dt}, \boldsymbol{v}_h\right) + B(\rho(\Phi_h^{n-1})\boldsymbol{u}_h^{n-1}, \boldsymbol{u}_h^n, \boldsymbol{v}_h) + (\nu(\Phi_h^n)D(\boldsymbol{u}_h^n), D(\boldsymbol{v}_h))\\ &\quad + \frac{dt}{\epsilon}(\nabla\cdot\boldsymbol{u}_h^n, \nabla\cdot\boldsymbol{v}_h) + a_{stab}(\boldsymbol{m}_h^{n-1}, \boldsymbol{u}_h^n, \boldsymbol{v}_h) + \frac{\lambda}{\varepsilon}(\Phi_h^{n-1}\nabla W_h^n, \boldsymbol{v}_h)\\ &= (p_h^{n-1}, \nabla\cdot\boldsymbol{v}_h) + \mu((\boldsymbol{m}_h^{n-1}\cdot\nabla)\boldsymbol{h}_h^{n-1}, \boldsymbol{v}_h) + \mu(\boldsymbol{m}_h^{n-1}\times\nabla\times\boldsymbol{h}_h^{n-1}, \boldsymbol{v}_h),\end{aligned} \tag{41}$$

where a_{stab} [83] includes two extra first-order stabilization terms that read as

$$a_{stab}(\boldsymbol{m}_h^{n-1}, \boldsymbol{u}_h^n, \boldsymbol{v}_h) = \mu dt((\boldsymbol{u}_h^n\cdot\nabla)\boldsymbol{m}_h^{n-1}, (\boldsymbol{v}_h\cdot\nabla)\boldsymbol{m}_h^{n-1}) + \mu dt((\nabla\cdot\boldsymbol{u}_h^n)\boldsymbol{m}_h^{n-1}, (\nabla\cdot\boldsymbol{v}_h)\boldsymbol{m}_h^{n-1}). \tag{42}$$

Step 3. Update p_h^n from

$$p_h^n = p_h^{n-1} - \frac{dt}{\epsilon}\nabla\cdot\boldsymbol{u}_h^n, \tag{43}$$

where $0 < \epsilon \ll 1$ is the artificial compressibility parameter.

Step 4. Set $\boldsymbol{h}_h^n = \nabla\varphi_h^n$, and find $(\tilde{\boldsymbol{m}}_h^n, \varphi_h^n) \in \boldsymbol{N}_h \times Z_h$ such that for all $(\tilde{\boldsymbol{c}}_h, \psi_h) \in \boldsymbol{N}_h \times Z_h$

$$(d_t\tilde{\boldsymbol{m}}_h^n, \tilde{\boldsymbol{c}}_h) + \frac{1}{\tau}(\tilde{\boldsymbol{m}}_h^n, \tilde{\boldsymbol{c}}_h) - \frac{1}{\tau}(\chi(\Phi_h^n)\boldsymbol{h}_h^n, \tilde{\boldsymbol{c}}_h) = -((\boldsymbol{u}_h^n\cdot\nabla)\boldsymbol{m}_h^{n-1}, \tilde{\boldsymbol{c}}_h) - ((\nabla\cdot\boldsymbol{u}_h^n)\boldsymbol{m}_h^{n-1}, \tilde{\boldsymbol{c}}_h), \tag{44}$$

$$\frac{1}{\tau}(\nabla\varphi_h^n, \nabla\psi_h) + (d_t\nabla\varphi_h^n, \nabla\psi_h) + \frac{1}{\tau}(\tilde{\boldsymbol{m}}_h^n, \nabla\psi_h) + (d_t\tilde{\boldsymbol{m}}_h^n, \nabla\psi_h) = \frac{1}{\tau}(\boldsymbol{h}_a^n, \nabla\psi_h) + (d_t\boldsymbol{h}_a^n, \nabla\psi_h). \tag{45}$$

Step 5. Find $\boldsymbol{m}_h^n \in \boldsymbol{N}_h$ such that for all $\boldsymbol{c}_h \in \boldsymbol{N}_h$

$$(d_t\boldsymbol{m}_h^n, \boldsymbol{c}_h) + B(\boldsymbol{u}_h^n, \boldsymbol{m}_h^n, \boldsymbol{c}_h) + \frac{1}{\tau}(\boldsymbol{m}_h^n, \boldsymbol{c}_h) = \frac{1}{\tau}(\chi(\Phi_h^n)\nabla\varphi_h^n, \boldsymbol{c}_h). \tag{46}$$

In the rest of this section, we will discuss about the properties of this scheme, starting from several remarks.

Remark 4.1. *Aiming at the nonlinear potential $f(\Phi)$, we use the stabilized explicit method to discretize it [38,84–88]. The term $f(\Phi)$ is explicitly discretized and the stabilization term $S(\Phi_h^n - \Phi_h^{n-1}, w_h)$ is added in (40). The error that this term introduces is of order $Sdt\Phi_t(\cdot)$. Aiming at the nonlinear terms $\nabla\cdot(\boldsymbol{u}\Phi)$ and $\frac{\lambda}{\varepsilon}\Phi\nabla W$, we add an explicit stabilization term $\frac{\lambda dt}{2\varepsilon}(\frac{1}{\sigma_h^{n-1}}\Phi_h^{n-1}\nabla W_h^n, \frac{1}{\sigma_h^{n-1}}\Phi_h^{n-1}\nabla\phi_h)$ to decouple the calculations of $\boldsymbol{u}$ and (Φ, W) in (39), inspired by [38,85]. Furthermore, in (41) we apply implicit-explicit treatment to deal with the fluid convection and Kelvin force, add two extra consistent terms $\frac{dt}{\epsilon}(\nabla\cdot\boldsymbol{u}_h^n, \nabla\cdot\boldsymbol{v}_h)$, $\mu(\boldsymbol{m}_h^{n-1}\times\nabla\times\boldsymbol{h}_h^{n-1}, \boldsymbol{v}_h)$ which are zero terms at the continuous level and two extra first-order stabilization terms $a_{stab}(\boldsymbol{m}_h^{n-1}, \boldsymbol{u}_h^n, \boldsymbol{v}_h)$. These play an important role in obtaining the energy stability.*

Remark 4.2. *In view of the strong coupling of velocity and pressure, we use the artificial compressibility method to decouple the calculation for velocity and pressure [76,89,90]. The regularization term ϵp_t is added in (43), so that the numerical scheme does not impose any artificial boundary conditions on the pressure. The $\boldsymbol{u}$ is directly solved in Step 2. And then one can solve $\epsilon(d_tp_h^n, q_h) + (\nabla\cdot\boldsymbol{u}_h^n, q_h) = 0$ with $q_h \in Q_h$ for p.*

Remark 4.3. *To avoid taking two test functions, we are inspired by [38] to introduce an auxiliary intermediate variable in the Step 4. For the convective term in (46), we use the trilinear form $B(\boldsymbol{u}_h^n, \boldsymbol{m}_h^n, \boldsymbol{c}_h)$. But in (44), we still use $((\boldsymbol{u}_h^n\cdot\nabla)\boldsymbol{m}_h^{n-1}, \tilde{\boldsymbol{c}}_h)$ and minus an extra consistent term $((\nabla\cdot\boldsymbol{u}_h^n)\boldsymbol{m}_h^{n-1}, \tilde{\boldsymbol{c}}_h)$, which is a zero term at the continuous level.*

As a matter of fact, based on the above three remarks, the scheme (38)–(46) is a linear and decoupled scheme. At each time step, we only need to compute five linear equations. In the following, we prove the unique solvability of this scheme.

Theorem 4.1. *For any $dt > 0$ and $h > 0$, the linear, decoupled and fully scheme (38)–(46) is uniquely solvable at each time step.*

Proof. From the above detailed implementation process, we just need to prove the existence and uniqueness of each sub-problem for the proposed scheme (38)–(46). Since they are finite dimensional, it is only necessary to prove that the following five homogeneous problems have only zero solution:

(I) Find $(\Phi_h^n, W_h^n) \in Y_h \times Y_h$ such that

$$\frac{1}{dt}(\Phi_h^n, \phi_h) + M(\nabla W_h^n, \nabla \phi_h) + \frac{\lambda dt}{2\varepsilon}\left(\frac{1}{\sigma_h^{n-1}}\Phi_h^{n-1}\nabla W_h^n, \frac{1}{\sigma_h^{n-1}}\Phi_h^{n-1}\nabla \phi_h\right) = 0, \tag{47a}$$

$$(W_h^n, w_h) - \varepsilon(\nabla \Phi_h^n, \nabla w_h) - S(\Phi_h^n, w_h) = 0, \tag{47b}$$

for all $(\phi_h, w_h) \in Y_h \times Y_h$.

(II) Find $\boldsymbol{u}_h^n \in \boldsymbol{V}_h$ such that

$$\begin{aligned}&\frac{1}{dt}(\rho_h^{n-1}\boldsymbol{u}_h^n, \boldsymbol{v}_h) + B(\rho(\Phi_h^{n-1})\boldsymbol{u}_h^{n-1}, \boldsymbol{u}_h^n, \boldsymbol{v}_h) + (\nu(\Phi_h^n)D(\boldsymbol{u}_h^n), D(\boldsymbol{v}_h)) + \frac{dt}{\epsilon}(\nabla\cdot\boldsymbol{u}_h^n, \nabla\cdot\boldsymbol{v}_h)\\ &\quad + \mu dt((\boldsymbol{u}_h^n\cdot\nabla)\boldsymbol{m}_h^{n-1}, (\boldsymbol{v}_h\cdot\nabla)\boldsymbol{m}_h^{n-1}) + \mu dt((\nabla\cdot\boldsymbol{u}_h^n)\boldsymbol{m}_h^{n-1}, (\nabla\cdot\boldsymbol{v}_h)\boldsymbol{m}_h^{n-1}) = 0,\end{aligned} \tag{48}$$

for all $\boldsymbol{v}_h \in \boldsymbol{V}_h$.

(III) Find $p_h^n \in Q_h$ such that

$$(p_h^n, q_h) = 0, \tag{49}$$

for all $q_h \in Q_h$.

(IV) Find $(\tilde{\boldsymbol{m}}_h^n, \varphi_h^n) \in \boldsymbol{N}_h \times Z_h$ such that

$$\frac{1}{dt}(\tilde{\boldsymbol{m}}_h^n, \tilde{\boldsymbol{c}}_h) + \frac{1}{\tau}(\tilde{\boldsymbol{m}}_h^n, \tilde{\boldsymbol{c}}_h) - \frac{1}{\tau}(\chi(\Phi_h^n)\boldsymbol{h}_h^n, \tilde{\boldsymbol{c}}_h) = 0, \tag{50a}$$

$$\frac{1}{\tau}(\nabla\varphi_h^n, \nabla\psi_h) + \frac{1}{dt}(\nabla\varphi_h^n, \nabla\psi_h) + \frac{1}{\tau}(\tilde{\boldsymbol{m}}_h^n, \nabla\psi_h) + \frac{1}{dt}(\tilde{\boldsymbol{m}}_h^n, \nabla\psi_h) = 0, \tag{50b}$$

for all $(\tilde{\boldsymbol{c}}_h, \psi_h) \in \boldsymbol{N}_h \times Z_h$.

(V) Find $\boldsymbol{m}_h^n \in \boldsymbol{N}_h$ such that

$$\frac{1}{dt}(\boldsymbol{m}_h^n, \boldsymbol{c}_h) + B(\boldsymbol{u}_h^n, \boldsymbol{m}_h^n, \boldsymbol{c}_h) + \frac{1}{\tau}(\boldsymbol{m}_h^n, \boldsymbol{c}_h) = 0, \tag{51}$$

for all $\boldsymbol{c}_h \in \boldsymbol{N}_h$.

By taking $(\phi_h, w_h) = (W_h^n, -\frac{1}{dt}\Phi_h^n)$ in (4.10), we obtain

$$\frac{1}{dt}(\Phi_h^n, W_h^n) + M\|\nabla W_h^n\|^2 + \frac{\lambda dt}{2\varepsilon}\|\frac{1}{\sigma_h^{n-1}}\Phi_h^{n-1}\nabla W_h^n\|^2 = 0, \tag{52}$$

$$-\frac{1}{dt}(W_h^n, \Phi_h^n) + \frac{\varepsilon}{dt}\|\nabla\Phi_h^n\|^2 + \frac{S}{dt}\|\Phi_h^n\|^2 = 0. \tag{53}$$

Summing up (52) and (53), we obtain

$$M\|\nabla W_h^n\|^2 + \frac{\lambda dt}{2\varepsilon}\|\frac{1}{\sigma_h^{n-1}}\Phi_h^{n-1}\nabla W_h^n\|^2 + \frac{\varepsilon}{dt}\|\nabla\Phi_h^n\|^2 + \frac{S}{dt}\|\Phi_h^n\|^2 = 0. \tag{54}$$

Thereby, we get $\Phi_h^n = W_h^n = 0$. Letting $\boldsymbol{v}_h = \boldsymbol{u}_h^n$ in (48), we derive

$$\begin{aligned}&\frac{1}{dt}\|\sigma_h^{n-1}\boldsymbol{u}_h^n\|^2 + \|\sqrt{\nu(\Phi_h^n)}D(\boldsymbol{u}_h^n)\|^2 + \mu dt\|(\boldsymbol{u}_h^n\cdot\nabla)\boldsymbol{m}_h^{n-1}\|^2\\ &\quad + \mu dt\|(\nabla\cdot\boldsymbol{u}_h^n)\boldsymbol{m}_h^{n-1}\|^2 + \frac{dt}{\epsilon}\|\nabla\cdot\boldsymbol{u}_h^n\|^2 = 0,\end{aligned} \tag{55}$$

which means $\boldsymbol{u}_h^n = \boldsymbol{0}$. Setting $q_h = p_h^n$ in (49), it is easy obtain $p_h^n = 0$. Taking $(\tilde{\boldsymbol{c}}_h, \psi_h) = (-\boldsymbol{h}_h^n, \varphi_h^n)$ in (4.13), and using $\boldsymbol{h}_h^n = \nabla\varphi_h^n$, we derive

$$-\frac{1}{dt}(\tilde{\boldsymbol{m}}_h^n, \boldsymbol{h}_h^n) - \frac{1}{\tau}(\tilde{\boldsymbol{m}}_h^n, \boldsymbol{h}_h^n) + \frac{1}{\tau}\|\sqrt{\chi(\Phi_h^n)}\boldsymbol{h}_h^n\|^2 = 0, \tag{56}$$

$$\frac{1}{\tau}\|\boldsymbol{h}_h^n\|^2 + \frac{1}{dt}\|\boldsymbol{h}_h^n\|^2 + \frac{1}{\tau}(\tilde{\boldsymbol{m}}_h^n, \boldsymbol{h}_h^n) + \frac{1}{dt}(\tilde{\boldsymbol{m}}_h^n, \boldsymbol{h}_h^n) = 0. \tag{57}$$

Thus, by summing up (56) and (57), we obtain

$$\frac{1}{\tau}\|\boldsymbol{h}_h^n\|^2 + \frac{1}{dt}\|\boldsymbol{h}_h^n\|^2 + \frac{1}{\tau}\|\sqrt{\chi(\Phi_h^n)}\boldsymbol{h}_h^n\|^2 = 0, \tag{58}$$

which implies $\boldsymbol{h}_h^n = 0$. Then we obtain

$$\frac{1}{dt}(\tilde{\boldsymbol{m}}_h^n, \tilde{\boldsymbol{c}}_h) + \frac{1}{\tau}(\tilde{\boldsymbol{m}}_h^n, \tilde{\boldsymbol{c}}_h) = 0. \tag{59}$$

Obviously, taking $\tilde{\boldsymbol{c}}_h = \tilde{\boldsymbol{m}}_h^n$ in (59), we derive $\tilde{\boldsymbol{m}}_h^n = \boldsymbol{0}$. Setting $\boldsymbol{c}_h = \boldsymbol{m}_h^n$ in (51), it is easy to obtain $\boldsymbol{m}_h^n = \boldsymbol{0}$. Therefore, the five homogeneous problems (4.10)–(51) only have zero solution. This concludes the proof. □

Next, we recall an important lemma to derive the unconditional energy stability of the scheme (38)–(46).

Lemma 4.1 ([38]). *Let $\boldsymbol{m}, \boldsymbol{u} \in \boldsymbol{L^2}(\Omega)$, $\boldsymbol{h} \in \boldsymbol{H^1}(\Omega)$. Then the following identity holds true*

$$((\boldsymbol{m}\cdot\nabla)\boldsymbol{h},\boldsymbol{u}) + (\boldsymbol{u}\times\boldsymbol{m}, \nabla\times\boldsymbol{h}) = ((\boldsymbol{u}\cdot\nabla)\boldsymbol{h},\boldsymbol{m}). \tag{60}$$

Theorem 4.2. *Choose $S \geq \frac{1}{4\epsilon}$. Then scheme (38)–(46) is unconditionally stable, and satisfies the following energy law:*

$$E_1(\Phi_h^N,\boldsymbol{u}_h^N,p_h^N,\boldsymbol{m}_h^N,\boldsymbol{h}_h^N) + dt\sum_{n=1}^{N} G_1^n \leq E_1(\Phi_h^0,\boldsymbol{u}_h^0,p_h^0,\boldsymbol{m}_h^0,\boldsymbol{h}_h^0) + dt\sum_{n=1}^{N}\Big(\frac{\mu}{2\tau}\|\boldsymbol{h}_a^n\|^2 + \frac{\tau\mu}{2}\|d_t\boldsymbol{h}_a^n\|^2\Big), \tag{61}$$

where

$$\begin{aligned} E_1(\Phi_h^N,\boldsymbol{u}_h^N,p_h^N,\boldsymbol{m}_h^N,\boldsymbol{h}_h^N) = {}& \frac{\lambda}{2}\|\nabla\Phi_h^N\|^2 + \frac{1}{2}\|\sigma_h^{N-1}\boldsymbol{u}_h^N\|^2 + \frac{\epsilon}{2}\|p_h^N\|^2 + \frac{\mu}{2}\|\boldsymbol{h}_h^N\|^2 \\ & + \frac{\mu}{2\chi_0}\|\boldsymbol{m}_h^N\|^2 + \frac{\lambda}{\epsilon}(F(\Phi_h^N),1) \end{aligned} \tag{62}$$

and

$$\begin{aligned} G_1^n = {}& \frac{\lambda M}{\epsilon}\|\nabla W_h^n\|^2 + \frac{\lambda}{2dt}\|\nabla(\Phi_h^n-\Phi_h^{n-1})\|^2 + \frac{\epsilon}{2dt}\|p_h^n-p_h^{n-1}\|^2 + \frac{\mu}{2\chi_0 dt}\|\boldsymbol{m}_h^n-\boldsymbol{m}_h^{n-1}\|^2 \\ & + \|\sqrt{\nu(\Phi_h^n)}D(\boldsymbol{u}_h^n)\|^2 + \frac{3\mu}{4\tau\chi_0}\|\boldsymbol{m}_h^n\|^2. \end{aligned} \tag{63}$$

Proof. Setting $\phi_h = \frac{\lambda}{\epsilon}W_h^n$ in (39) and $w_h = -\frac{\lambda}{\epsilon}d_t\Phi_h^n$ in (40), respectively, we deduce

$$\frac{\lambda}{\epsilon}(d_t\Phi_h^n, W_h^n) + \frac{\lambda M}{\epsilon}\|\nabla W_h^n\|^2 + \frac{\lambda^2 dt}{2\epsilon^2}\|\frac{1}{\sigma_h^{n-1}}\Phi_h^{n-1}\nabla W_h^n\|^2 = \frac{\lambda}{\epsilon}(\boldsymbol{u}_h^{n-1}\Phi_h^{n-1},\nabla W_h^n), \tag{64}$$

$$\begin{aligned} & -\frac{\lambda}{\epsilon}(W_h^n, d_t\Phi_h^n) + \frac{\lambda}{2dt}(\|\nabla\Phi_h^n\|^2 - \|\nabla\Phi_h^{n-1}\|^2 + \|\nabla(\Phi_h^n-\Phi_h^{n-1})\|^2) + \frac{S\lambda}{\epsilon dt}\|\Phi_h^n-\Phi_h^{n-1}\|^2 \\ & = -\frac{\lambda}{\epsilon}(f(\Phi_h^{n-1}), d_t\Phi_h^n). \end{aligned} \tag{65}$$

Summing up (64) and (65), we have

$$\begin{aligned} & \frac{\lambda M}{\epsilon}\|\nabla W_h^n\|^2 + \frac{\lambda^2 dt}{2\epsilon^2}\|\frac{1}{\sigma_h^{n-1}}\Phi_h^{n-1}\nabla W_h^n\|^2 + \frac{\lambda}{2dt}(\|\nabla\Phi_h^n\|^2 - \|\nabla\Phi_h^{n-1}\|^2 + \|\nabla(\Phi_h^n-\Phi_h^{n-1})\|^2) \\ & + \frac{\lambda S}{\epsilon dt}\|\Phi_h^n-\Phi_h^{n-1}\|^2 = \frac{\lambda}{\epsilon}(\boldsymbol{u}_h^{n-1}\Phi_h^{n-1},\nabla W_h^n) - \frac{\lambda}{\epsilon}(f(\Phi_h^{n-1}), d_t\Phi_h^n). \end{aligned} \tag{66}$$

Letting $\boldsymbol{v}_h = \boldsymbol{u}_h^n$ in (41), we derive

$$\begin{aligned} & \frac{1}{2dt}(\|\sigma_h^{n-1}\boldsymbol{u}_h^n\|^2 - \|\sigma_h^{n-1}\boldsymbol{u}_h^{n-1}\|^2 + \|\sigma_h^{n-1}(\boldsymbol{u}_h^n-\boldsymbol{u}_h^{n-1})\|^2) + \|\sqrt{\nu(\Phi_h^n)}D(\boldsymbol{u}_h^n)\|^2 + \frac{dt}{\epsilon}\|\nabla\cdot\boldsymbol{u}_h^n\|^2 \\ & + \mu dt\|(\boldsymbol{u}_h^n\cdot\nabla)\boldsymbol{m}_h^{n-1}\|^2 + \mu dt\|(\nabla\cdot\boldsymbol{u}_h^n)\boldsymbol{m}_h^{n-1}\|^2 = (p_h^{n-1},\nabla\cdot\boldsymbol{u}_h^n) - \frac{\lambda}{\epsilon}(\Phi_h^{n-1}\nabla W_h^n,\boldsymbol{u}_h^n) \\ & + \mu((\boldsymbol{m}_h^{n-1}\cdot\nabla)\boldsymbol{h}_h^{n-1},\boldsymbol{u}_h^n) + \mu(\boldsymbol{m}_h^{n-1}\times\nabla\times\boldsymbol{h}_h^{n-1},\boldsymbol{u}_h^n). \end{aligned} \tag{67}$$

We rewrite (43) as the following equivalent form:

$$\frac{\epsilon}{dt}(p_h^n-p_h^{n-1}) + \nabla\cdot\boldsymbol{u}_h^n = 0. \tag{68}$$

By taking the L^2 inner product of the above equation with p_h^n on both sides, we obtain

$$\frac{\epsilon}{2dt}(\|p_h^n\|^2 - \|p_h^{n-1}\|^2 + \|p_h^n-p_h^{n-1}\|^2) + (\nabla\cdot\boldsymbol{u}_h^n, p_h^n) = 0. \tag{69}$$

Combining (67) and (69), we get

$$\begin{aligned} & \frac{1}{2dt}(\|\sigma_h^{n-1}\boldsymbol{u}_h^n\|^2 - \|\sigma_h^{n-1}\boldsymbol{u}_h^{n-1}\|^2 + \|\sigma_h^{n-1}(\boldsymbol{u}_h^n-\boldsymbol{u}_h^{n-1})\|^2) + \frac{\epsilon}{2dt}(\|p_h^n\|^2 - \|p_h^{n-1}\|^2 + \|p_h^n-p_h^{n-1}\|^2) \\ & + \|\sqrt{\nu(\Phi_h^n)}D(\boldsymbol{u}_h^n)\|^2 + \mu dt\|(\boldsymbol{u}_h^n\cdot\nabla)\boldsymbol{m}_h^{n-1}\|^2 + \mu dt\|(\nabla\cdot\boldsymbol{u}_h^n)\boldsymbol{m}_h^{n-1}\|^2 \\ & = -\frac{\lambda}{\epsilon}(\Phi_h^{n-1}\nabla W_h^n,\boldsymbol{u}_h^n) + \mu((\boldsymbol{m}_h^{n-1}\cdot\nabla)\boldsymbol{h}_h^{n-1},\boldsymbol{u}_h^n) + \mu(\boldsymbol{m}_h^{n-1}\times\nabla\times\boldsymbol{h}_h^{n-1},\boldsymbol{u}_h^n). \end{aligned} \tag{70}$$

Letting $\tilde{\boldsymbol{c}}_h = -\mu\boldsymbol{h}_h^n$ in (44), we derive

$$\begin{aligned} & -\mu(d_t\tilde{\boldsymbol{m}}_h^n,\boldsymbol{h}_h^n) - \frac{\mu}{\tau}(\tilde{\boldsymbol{m}}_h^n,\boldsymbol{h}_h^n) + \frac{\mu}{\tau}\|\sqrt{\chi(\Phi_h^n)}\boldsymbol{h}_h^n\|^2 \\ & = \mu((\boldsymbol{u}_h^n\cdot\nabla)\boldsymbol{m}_h^{n-1},\boldsymbol{h}_h^n) + \mu((\nabla\cdot\boldsymbol{u}_h^n)\boldsymbol{m}_h^{n-1},\boldsymbol{h}_h^n). \end{aligned} \tag{71}$$

By taking $\psi_h = \mu\varphi_h^n$ in (45), and applying $\boldsymbol{h}_h^n = \nabla\varphi_h^n$, we have

$$\begin{aligned}&\frac{\mu}{\tau}\|\boldsymbol{h}_h^n\|^2 + \frac{\mu}{2dt}(\|\boldsymbol{h}_h^n\|^2 - \|\boldsymbol{h}_h^{n-1}\|^2 + \|\boldsymbol{h}_h^n - \boldsymbol{h}_h^{n-1}\|^2) + \frac{\mu}{\tau}(\tilde{\boldsymbol{m}}_h^n, \boldsymbol{h}_h^n) + \mu(d_t\tilde{\boldsymbol{m}}_h^n, \boldsymbol{h}_h^n)\\ &= \frac{\mu}{\tau}(\boldsymbol{h}_a^n, \boldsymbol{h}_h^n) + \mu(d_t\boldsymbol{h}_a^n, \boldsymbol{h}_h^n).\end{aligned} \tag{72}$$

Thus, summing up (71) and (72), we get

$$\begin{aligned}&\frac{\mu}{2dt}(\|\boldsymbol{h}_h^n\|^2 - \|\boldsymbol{h}_h^{n-1}\|^2 + \|\boldsymbol{h}_h^n - \boldsymbol{h}_h^{n-1}\|^2) + \frac{\mu}{\tau}\|\sqrt{\chi(\Phi_h^n)}\boldsymbol{h}_h^n\|^2 + \frac{\mu}{\tau}\|\boldsymbol{h}_h^n\|^2\\ &= \mu((\boldsymbol{u}_h^n\cdot\nabla)\boldsymbol{m}_h^{n-1}, \boldsymbol{h}_h^n) + \mu((\nabla\cdot\boldsymbol{u}_h^n)\boldsymbol{m}_h^{n-1}, \boldsymbol{h}_h^n) + \frac{\mu}{\tau}(\boldsymbol{h}_a^n, \boldsymbol{h}_h^n) + \mu(d_t\boldsymbol{h}_a^n, \boldsymbol{h}_h^n).\end{aligned} \tag{73}$$

Setting $\boldsymbol{c}_h = \frac{\mu}{\chi_0}\boldsymbol{m}_h^n$ in (46), and from $\boldsymbol{h}_h^n = \nabla\varphi_h^n$, we deduce

$$\frac{\mu}{2\chi_0 dt}(\|\boldsymbol{m}_h^n\|^2 - \|\boldsymbol{m}_h^{n-1}\|^2 + \|\boldsymbol{m}_h^n - \boldsymbol{m}_h^{n-1}\|^2) + \frac{\mu}{\tau\chi_0}\|\boldsymbol{m}_h^n\|^2 = \frac{\mu}{\tau\chi_0}(\chi(\Phi_h^n)\boldsymbol{h}_h^n, \boldsymbol{m}_h^n). \tag{74}$$

Summing up (66), (70), (73) and (74), we deduce

$$\begin{aligned}&\frac{\lambda M}{\varepsilon}\|\nabla W_h^n\|^2 + \frac{\lambda}{2dt}(\|\nabla\Phi_h^n\|^2 - \|\nabla\Phi_h^{n-1}\|^2 + \|\nabla(\Phi_h^n - \Phi_h^{n-1})\|^2) + \frac{\lambda^2 dt}{2\varepsilon^2}\|\frac{1}{\sigma_h^{n-1}}\Phi_h^{n-1}\nabla W_h^n\|^2\\ &+ \frac{\lambda S}{\varepsilon dt}\|\Phi_h^n - \Phi_h^{n-1}\|^2 + \frac{1}{2dt}(\|\sigma_h^{n-1}\boldsymbol{u}_h^n\|^2 - \|\sigma_h^{n-1}\boldsymbol{u}_h^{n-1}\|^2 + \|\sigma_h^{n-1}(\boldsymbol{u}_h^n - \boldsymbol{u}_h^{n-1})\|^2)\\ &+ \|\sqrt{\nu(\Phi_h^n)}D(\boldsymbol{u}_h^n)\|^2 + \frac{\epsilon}{2dt}(\|p_h^n\|^2 - \|p_h^{n-1}\|^2 + \|p_h^n - p_h^{n-1}\|^2) + \mu dt\|(\boldsymbol{u}_h^n\cdot\nabla)\boldsymbol{m}_h^{n-1}\|^2\\ &+ \mu dt\|(\nabla\cdot\boldsymbol{u}_h^n)\boldsymbol{m}_h^{n-1}\|^2 + \frac{\mu}{2dt}(\|\boldsymbol{h}_h^n\|^2 - \|\boldsymbol{h}_h^{n-1}\|^2 + \|\boldsymbol{h}_h^n - \boldsymbol{h}_h^{n-1}\|^2) + \frac{\mu}{\tau}\|\sqrt{\chi(\Phi_h^n)}\boldsymbol{h}_h^n\|^2\\ &+ \frac{\mu}{\tau}\|\boldsymbol{h}_h^n\|^2 + \frac{\mu}{\tau\chi_0}\|\boldsymbol{m}_h^n\|^2 + \frac{\mu}{2\chi_0 dt}(\|\boldsymbol{m}_h^n\|^2 - \|\boldsymbol{m}_h^{n-1}\|^2 + \|\boldsymbol{m}_h^n - \boldsymbol{m}_h^{n-1}\|^2)\\ =&\ \mu((\boldsymbol{m}_h^{n-1}\cdot\nabla)\boldsymbol{h}_h^{n-1}, \boldsymbol{u}_h^n) + \mu((\boldsymbol{u}_h^n\cdot\nabla)\boldsymbol{m}_h^{n-1}, \boldsymbol{h}_h^n) + \mu((\nabla\cdot\boldsymbol{u}_h^n)\boldsymbol{m}_h^{n-1}, \boldsymbol{h}_h^n)\\ &+ \mu(\boldsymbol{m}_h^{n-1}\times\nabla\times\boldsymbol{h}_h^{n-1}, \boldsymbol{u}_h^n)\ (I)\\ &+ \frac{\lambda}{\varepsilon}(\boldsymbol{u}_h^{n-1}\Phi_h^{n-1}, \nabla W_h^n) - \frac{\lambda}{\varepsilon}(\Phi_h^{n-1}\nabla W_h^n, \boldsymbol{u}_h^n)\ (II)\\ &+ \frac{\mu}{\tau}(\boldsymbol{h}_a^n, \boldsymbol{h}_h^n) + \mu(d_t\boldsymbol{h}_a^n, \boldsymbol{h}_h^n) + \frac{\mu}{\tau\chi_0}(\chi(\Phi_h^n)\boldsymbol{h}_h^n, \boldsymbol{m}_h^n)\ (III)\\ &- \frac{\lambda}{\varepsilon}(f(\Phi_h^{n-1}), d_t\Phi_h^n).\ (IV)\end{aligned} \tag{75}$$

Next, we estimate $I - IV$ on the right-hand side of (75) as follows.

Firstly, applying Young's inequality, Lemma 4.1, and integration by parts, we estimate I as

$$\begin{aligned}I =&\ \mu((\boldsymbol{m}_h^{n-1}\cdot\nabla)\boldsymbol{h}_h^{n-1}, \boldsymbol{u}_h^n) + \mu(\boldsymbol{m}_h^{n-1}\times\nabla\times\boldsymbol{h}_h^{n-1}, \boldsymbol{u}_h^n) + \mu((\boldsymbol{u}_h^n\cdot\nabla)\boldsymbol{m}_h^{n-1}, \boldsymbol{h}_h^n)\\ &+ \mu((\nabla\cdot\boldsymbol{u}_h^n)\boldsymbol{m}_h^{n-1}, \boldsymbol{h}_h^n)\\ =&\ \mu((\boldsymbol{u}_h^n\cdot\nabla)\boldsymbol{h}_h^{n-1}, \boldsymbol{m}_h^{n-1}) + \mu((\boldsymbol{u}_h^n\cdot\nabla)\boldsymbol{m}_h^{n-1}, \boldsymbol{h}_h^n) + \mu((\nabla\cdot\boldsymbol{u}_h^n)\boldsymbol{m}_h^{n-1}, \boldsymbol{h}_h^n)\\ =&\ \mu((\boldsymbol{u}_h^n\cdot\nabla)(\boldsymbol{h}_h^{n-1} - \boldsymbol{h}_h^n), \boldsymbol{m}_h^{n-1})\\ =&\ -\mu((\boldsymbol{u}_h^n\cdot\nabla)\boldsymbol{m}_h^{n-1}, \boldsymbol{h}_h^{n-1} - \boldsymbol{h}_h^n) - \mu((\nabla\cdot\boldsymbol{u}_h^n)\boldsymbol{m}_h^{n-1}, \boldsymbol{h}_h^{n-1} - \boldsymbol{h}_h^n)\\ \le&\ \mu\|(\boldsymbol{u}_h^n\cdot\nabla)\boldsymbol{m}_h^{n-1}\|\ \|\boldsymbol{h}_h^{n-1} - \boldsymbol{h}_h^n\| + \mu\|(\nabla\cdot\boldsymbol{u}_h^n)\boldsymbol{m}_h^{n-1}\|\ \|\boldsymbol{h}_h^{n-1} - \boldsymbol{h}_h^n\|\\ \le&\ \mu dt\|(\boldsymbol{u}_h^n\cdot\nabla)\boldsymbol{m}_h^{n-1}\|^2 + \mu dt\|(\nabla\cdot\boldsymbol{u}_h^n)\boldsymbol{m}_h^{n-1}\|^2 + \frac{\mu}{2dt}\|\boldsymbol{h}_h^{n-1} - \boldsymbol{h}_h^n\|^2.\end{aligned} \tag{76}$$

Secondly, we estimate II as

$$\begin{aligned}II =&\ \frac{\lambda}{\varepsilon}(\boldsymbol{u}_h^{n-1}\Phi_h^{n-1}, \nabla W_h^n) - \frac{\lambda}{\varepsilon}(\Phi_h^{n-1}\nabla W_h^n, \boldsymbol{u}_h^n)\\ =&\frac{\lambda}{\varepsilon}(\frac{1}{\sigma_h^{n-1}}\Phi_h^{n-1}\nabla W_h^n, \sigma_h^{n-1}(\boldsymbol{u}_h^{n-1} - \boldsymbol{u}_h^n))\\ \le&\frac{\lambda}{\varepsilon}\|\frac{1}{\sigma_h^{n-1}}\Phi_h^{n-1}\nabla W_h^n\|\ \|\sigma_h^{n-1}(\boldsymbol{u}_h^{n-1} - \boldsymbol{u}_h^n)\|\\ \le&\frac{\lambda^2 dt}{2\varepsilon^2}\|\frac{1}{\sigma_h^{n-1}}\Phi_h^{n-1}\nabla W_h^n\|^2 + \frac{1}{2dt}\|\sigma_h^{n-1}(\boldsymbol{u}_h^n - \boldsymbol{u}_h^{n-1})\|^2.\end{aligned} \tag{77}$$

Thirdly, III is estimated as

$$\begin{aligned} III &= \frac{\mu}{\tau}(\boldsymbol{h}_a^n, \boldsymbol{h}_h^n) + \mu(d_t\boldsymbol{h}_a^n, \boldsymbol{h}_h^n) + \frac{\mu}{\tau\chi_0}(\chi(\Phi_h^n)\boldsymbol{h}_h^n, \boldsymbol{m}_h^n) \\ &\le \frac{\mu}{\tau}\|\boldsymbol{h}_a^n\|\,\|\boldsymbol{h}_h^n\| + \mu\|d_t\boldsymbol{h}_a^n\|\,\|\boldsymbol{h}_h^n\| + \frac{\mu}{\tau\chi_0}\|\sqrt{\chi(\Phi_h^n)}\boldsymbol{h}_h^n\|\,\|\sqrt{\chi(\Phi_h^n)}\boldsymbol{m}_h^n\| \\ &\le \frac{\mu}{2\tau}\|\boldsymbol{h}_h^n\|^2 + \frac{\mu}{2\tau}\|\boldsymbol{h}_a^n\|^2 + \frac{\mu}{2\tau}\|\boldsymbol{h}_h^n\|^2 + \frac{\tau\mu}{2}\|d_t\boldsymbol{h}_a^n\|^2 + \frac{\mu}{\tau}\|\sqrt{\chi(\Phi_h^n)}\boldsymbol{h}_h^n\|^2 + \frac{\mu}{4\tau\chi_0^2}\|\sqrt{\chi(\Phi_h^n)}\boldsymbol{m}_h^n\|^2 \\ &\le \frac{\mu}{\tau}\|\boldsymbol{h}_h^n\|^2 + \frac{\mu}{2\tau}\|\boldsymbol{h}_a^n\|^2 + \frac{\tau\mu}{2}\|d_t\boldsymbol{h}_a^n\|^2 + \frac{\mu}{\tau}\|\sqrt{\chi(\Phi_h^n)}\boldsymbol{h}_h^n\|^2 + \frac{\mu}{4\tau\chi_0}\|\boldsymbol{m}_h^n\|^2. \end{aligned} \tag{78}$$

Finally, we apply the Taylor expansion for $F(\Phi_h^n)$ to estimate the term IV. Then there exists a aparameter θ such that

$$F(\Phi_h^n) - F(\Phi_h^{n-1}) = f(\Phi_h^{n-1})(\Phi_h^n - \Phi_h^{n-1}) + \frac{1}{2}f'(\theta)(\Phi_h^n - \Phi_h^{n-1})^2. \tag{79}$$

From $|F''(\Phi)| = |f'(\Phi)| \le \frac{1}{2\varepsilon}$, we derive

$$\begin{aligned} (d_tF(\Phi_h^n), 1) &= \frac{1}{dt}(F(\Phi_h^n) - F(\Phi_h^{n-1}), 1) \\ &= (f(\Phi_h^{n-1}), d_t\Phi_h^n) + \frac{1}{2dt}(f'(\theta), (\Phi_h^n - \Phi_h^{n-1})^2) \\ &\le (f(\Phi_h^{n-1}), d_t\Phi_h^n) + \frac{1}{4\varepsilon dt}\|\Phi_h^n - \Phi_h^{n-1}\|^2, \end{aligned} \tag{80}$$

which implies

$$IV = -\frac{\lambda}{\varepsilon}(f(\Phi_h^{n-1}), d_t\Phi_h^n) \le -\frac{\lambda}{\varepsilon}(d_tF(\Phi_h^n), 1) + \frac{\lambda}{4\varepsilon^2 dt}\|\Phi_h^n - \Phi_h^{n-1}\|^2. \tag{81}$$

By combining (75)–(78) and (81), we have

$$\begin{aligned} &\frac{\lambda M}{\varepsilon}\|\nabla W_h^n\|^2 + \frac{\lambda}{2dt}(\|\nabla\Phi_h^n\|^2 - \|\nabla\Phi_h^{n-1}\|^2 + \|\nabla(\Phi_h^n - \Phi_h^{n-1})\|^2) + \|\sqrt{\nu(\Phi_h^n)}D(\boldsymbol{u}_h^n)\|^2 + \frac{3\mu}{4\tau\chi_0}\|\boldsymbol{m}_h^n\|^2 \\ &+ \frac{1}{2dt}(\|\sigma_h^{n-1}\boldsymbol{u}_h^n\|^2 - \|\sigma_h^{n-1}\boldsymbol{u}_h^{n-1}\|^2) + \frac{\epsilon}{2dt}(\|p_h^n\|^2 - \|p_h^{n-1}\|^2 + \|p_h^n - p_h^{n-1}\|^2) + \frac{\lambda}{\varepsilon}(d_tF(\Phi_h^n), 1) \\ &+ \frac{\mu}{2dt}(\|\boldsymbol{h}_h^n\|^2 - \|\boldsymbol{h}_h^{n-1}\|^2) + \frac{\mu}{2\chi_0 dt}(\|\boldsymbol{m}_h^n\|^2 - \|\boldsymbol{m}_h^{n-1}\|^2 + \|\boldsymbol{m}_h^n - \boldsymbol{m}_h^{n-1}\|^2) \\ &+ \frac{\lambda}{\varepsilon dt}(S - \frac{1}{4\varepsilon})\|\Phi_h^n - \Phi_h^{n-1}\|^2 \le \frac{\mu}{2\tau}\|\boldsymbol{h}_a^n\|^2 + \frac{\tau\mu}{2}\|d_t\boldsymbol{h}_a^n\|^2. \end{aligned} \tag{82}$$

It is worth noting that $\boldsymbol{h}_a$ is a given external magnetic field acting as a source term and may change over time. Therefore, the symbol $\boldsymbol{h}_a^n$ is taken as a known term in the numerical scheme, and its value may change with time. Thus, summing up from $n = 1$ to N for inequality (82), and from $S \ge \frac{1}{4\varepsilon}$, we obtain

$$E_1(\Phi_h^N, \boldsymbol{u}_h^N, p_h^N, \boldsymbol{m}_h^N, \boldsymbol{h}_h^N) + dt\sum_{n=1}^{N} G_1^n \le E_1(\Phi_h^0, \boldsymbol{u}_h^0, p_h^0, \boldsymbol{m}_h^0, \boldsymbol{h}_h^0) + dt\sum_{n=1}^{N}(\frac{\mu}{2\tau}\|\boldsymbol{h}_a^n\|^2 + \frac{\tau\mu}{2}\|d_t\boldsymbol{h}_a^n\|^2). \tag{83}$$

□

5. Numerical experiments

In this section, a series of two-dimensional numerical experiments, including an accuracy test, deformation of a ferrofluid droplet, one or two air bubbles rising in ferrofluids, a controllable ferrofluid droplet in a Y-shape domain, and the Rosensweig instability under uniformly or nonuniformly applied magnetic field, are performed to illustrate various features of the proposed model and scheme. Moreover, we choose $S = \frac{1}{4\varepsilon}$ in all numerical tests.

5.1. Accuracy test

In this part, the example is used to verify the convergence rates in space. We set the calculational domain as $\Omega = (0,1)\times(0,1)$. The model physicial parameters are given as $\varepsilon = \lambda = 0.1$, $M = 0.05$, $\rho_f = 3$, $\rho_w = \nu_f = \nu_w = \mu = \tau = \chi_0 = \epsilon = 1$. Moreover, we choose forcing functions and boundary functions [38,39] such that the exact solutions of the system (2.13) with Dirichlet boundary conditions can be chosen as

$$\begin{cases} \Phi(t,\boldsymbol{x}) = 0.5\sin(t)\cos(\pi x)\cos(\pi y) + 0.5, \\ \boldsymbol{u}(t,\boldsymbol{x}) = (\sin(t)\sin(\pi x)\sin(\pi(y+0.5)), \sin(t)\cos(\pi x)\cos(\pi(y+0.5))^{\mathrm{t}}, \\ p(t,\boldsymbol{x}) = \sin(t)(2x-1)(2y-1), \\ \varphi(t,\boldsymbol{x}) = \sin(t)(x-0.5)y, \\ \boldsymbol{m}(t,\boldsymbol{x}) = (\sin(t+y), \sin(t+x))^{\mathrm{t}}. \end{cases} \tag{84}$$

Table 1
Numerical errors and convergence rates for proposed scheme (38)–(46).

h	$\|\Phi-\Phi_h\|$	Order	$\|\Phi-\Phi_h\|_{H^1}$	Order	$\|W-W_h\|$	Order	$\|W-W_h\|_{H^1}$	Order
1/8	5.27 e-03	–	1.05 e-01	–	7.34 e-03	–	8.65 e-02	–
1/16	1.40 e-03	1.91	5.24 e-02	1.01	2.03 e-03	1.85	4.15 e-02	1.06
1/32	3.56 e-04	1.98	2.61 e-02	1.00	5.21 e-04	1.96	2.04 e-02	1.02
1/64	8.95 e-05	1.99	1.31 e-02	1.00	1.31 e-04	1.99	1.01 e-02	1.01
h	$\|\boldsymbol{u}-\boldsymbol{u}_h\|$	Order	$\|\boldsymbol{u}-\boldsymbol{u}_h\|_{H^1}$	Order	$\|p-p_h\|$	Order	$\|p-p_h\|_{H^1}$	Order
1/8	1.11 e-03	–	2.35 e-02	–	2.28 e-03	–	1.38 e-01	–
1/16	2.67 e-04	2.06	5.90 e-03	1.99	5.71 e-04	2.00	6.92 e-02	1.00
1/32	6.62 e-05	2.02	1.48 e-03	1.99	1.43 e-04	2.00	3.46 e-02	1.00
1/64	1.65 e-05	2.00	3.69 e-04	1.99	3.56 e-05	2.00	1.73 e-02	0.99
h	$\|\boldsymbol{m}-\boldsymbol{m}_h\|$	Order	$\|\boldsymbol{m}-\boldsymbol{m}_h\|_{H^1}$	Order	$\|\varphi-\varphi_h\|$	Order	$\|\varphi-\varphi_h\|_{H^1}$	Order
1/8	3.38 e-03	–	4.60 e-02	–	1.04 e-04	–	8.11 e-04	–
1/16	8.87 e-04	1.93	2.21 e-02	1.06	2.79 e-05	1.89	1.85 e-04	2.13
1/32	2.27 e-04	1.97	1.08 e-02	1.03	7.28 e-06	1.93	4.25 e-05	2.13
1/64	5.74 e-05	1.98	5.32 e-03	1.02	1.86 e-06	1.97	9.98 e-06	2.10

That is, the forcing functions are calculated by plugging these exact solutions into the system (2.5). The Dirichlet boundary functions are also obtained by restricting these exact solutions on the boundary.

We choose the finite element spaces (34) with $l_1 = 1,\ l_2 = l_3 = 2$. In this way, we expect the optimal convergence error estimates as follows:

$$\begin{aligned}
&\|\Phi(t_n)-\Phi_h^n\| + \|W(t_n)-W_h^n\| \lesssim dt + h^2,\ \|\Phi(t_n)-\Phi_h^n\|_{H^1} + \|W(t_n)-W_h^n\|_{H^1} \lesssim dt + h,\\
&\|\boldsymbol{u}(t_n)-\boldsymbol{u}_h^n\| \lesssim dt + h^3,\ \|\boldsymbol{u}(t_n)-\boldsymbol{u}_h^n\|_{H^1} + \|p(t_n)-p_h^n\| \lesssim dt + h^2,\ \|p(t_n)-p_h^n\|_{H^1} \lesssim dt + h,\\
&\|\varphi(t_n)-\varphi_h^n\| \lesssim dt + h^3,\ \|\varphi(t_n)-\varphi_h^n\|_{H^1} + \|\boldsymbol{m}(t_n)-\boldsymbol{m}_h^n\| \lesssim dt + h^2,\ \|\boldsymbol{m}(t_n)-\boldsymbol{m}_h^n\|_{H^1} \lesssim dt + h.
\end{aligned} \tag{85}$$

For convenience, we abbreviate $\|\varrho(t_n)-\varrho_h^n\|$ as $\|\varrho-\varrho_h\|$ for variables Φ, W, $\boldsymbol{u}$, p, $\boldsymbol{m}$ and φ.

To check the convergence orders of our scheme, we use $dt = h^2$ with terminal time $T = 0.5$ and refine the spatial grid size with $h = 2^{-i}$, where $i = 3, 4, 5$ and 6. Table 1 shows the spatial L^2-norm and H^1-norm errors and convergence rates for the proposed scheme (38)–(46). It is observed that the accuracy orders of Φ, W, $\boldsymbol{u}$, p, $\boldsymbol{m}$ and φ in L^2-norm are $O(h^2)$, the accuracy orders of Φ, W, p and $\boldsymbol{m}$ in H^1-norm are $O(h)$, and the accuracy orders of $\boldsymbol{u}$ and φ in H^1-norm are $O(h^2)$. These accuracy orders are consistent with the above expected convergence orders (85).

For phase field models, one major difficulty is how to resolve the transition layer. Otherwise artificial spurious oscillations may arise [91–93]. If we want to obtain better results in a timely fashion, calculations of phase-field models need certain types of mesh adaptivity. Therefore, we apply adaptive grid to address this issue. Compared with the uniform grid, the adaptive grid is more efficient. The implementation is done in Matlab [94]. Regarding the error indicators, we resort to the simplest element indicator η_K:

$$\eta_K^2 = h_K \int_{\partial K} \|\nabla\Phi_h\|^2 \mathrm{d}s, \quad \forall K \in \mathcal{T}_h, \tag{86}$$

where h_K is the diameter of the circumscribed circle of triangle K.

5.2. Deformation of a ferrofluid droplet under uniformly applied magnetic field

In this subsection, we simulate the deformation of a ferrofluid droplet suspended in a viscous media under the different external uniform magnetic field $\boldsymbol{h}_a$ [23]. The equilibrium shape of the ferrofluid droplet is determined by the ratio of magnetic effect to surface tension effect, which can be characterized by the magnetic Bond number:

$$Bo_m = \frac{R_0 \mu H_0^2}{2\varsigma}, \tag{87}$$

where R_0 is a ferrofluid droplet of initial radius, H_0 is the external applied magnetic strength, and $\varsigma = \frac{\lambda}{\epsilon}$ is the coefficient of surface tension [95]. We recall a well known analytical expression, which relates the aspect ratio b/a of deformed ferrofluid droplet with the magnetic Bond number, as follows [23]:

$$Bo_m = \left[\frac{1}{\chi_0} + k\right]^2 \left(\frac{b}{a}\right)^{\frac{1}{3}} \left(2\frac{b}{a} - \left(\frac{b}{a}\right)^{-2} - 1\right). \tag{88}$$

Here $2a$ and $2b$ are the minor axis and the major axis of deformed ferrofluid droplet, respectively, k is called the demagnetizing factor:

$$k = \left(\frac{1-E^2}{2E^3}\right)\left(\ln\frac{1+E}{1-E} - 2E\right), \tag{89}$$

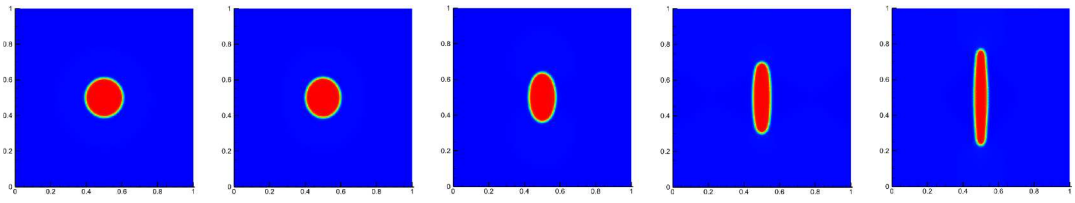

(a) H_0=0.5 (b) H_0=1 (c) H_0=2 (d) H_0=3 (e) H_0=4

Fig. 1. Snapshots of the phase field variable Φ under uniformly applied magnetic field with $H_0 = 0.5$, 1, 2, 3 and 4.

where $E = \sqrt{1 - a^2/b^2}$ is the eccentricity. Moreover, we use a linear combination of dipoles to generate the applied magnetizing field $\boldsymbol{h}_a$:

$$\boldsymbol{h}_a = \sum_s \alpha_s \nabla \kappa_s(\boldsymbol{x}), \tag{90}$$

where α_s is the intensity of the dipole,

$$\kappa_s(\boldsymbol{x}) = \frac{\boldsymbol{d} \cdot (\boldsymbol{x}_s - \boldsymbol{x})}{|\boldsymbol{x}_s - \boldsymbol{x}|^2}, \tag{91}$$

$|\boldsymbol{d}| = 1$ indicates the direction of the dipole and $\boldsymbol{x}_s$ is the dipole's position [37].

Consider the problem domain as $\Omega = (0, \mathrm{d}) \times (0, \mathrm{d})$. The equations (2.13) are non-dimensionalized by applying the following scaled variables [78,96]:

$$\tilde{\boldsymbol{u}} = \frac{\boldsymbol{u}}{\boldsymbol{u}_0}, \ \tilde{\boldsymbol{x}} = \frac{\boldsymbol{x}}{\mathrm{d}_0}, \ \tilde{t} = \frac{t}{t_0}, \ \tilde{\rho} = \frac{\rho}{\rho_0}, \tag{92}$$

where $\boldsymbol{u}_0 = \sqrt{\mathrm{d}|\boldsymbol{g}|}$, $\mathrm{d}_0 = \mathrm{d}$, $t_0 = \sqrt{\mathrm{d}/|\boldsymbol{g}|}$, $\rho_0 = \min(\rho_f, \rho_w)$, and $|\boldsymbol{g}|$ represents the magnitude of gravity. We also have

$$\nu(\Phi) = (\tilde{\nu}_f - \tilde{\nu}_w)\Phi + \tilde{\nu}_w, \ \rho(\Phi) = (\tilde{\rho}_f - \tilde{\rho}_w)\Phi + \tilde{\rho}_w, \tag{93}$$

where $\tilde{\rho}_f = \frac{\rho_f}{\rho_0}$, $\tilde{\rho}_w = \frac{\rho_w}{\rho_0}$, $\tilde{\nu}_f = \nu_f(\rho_0 \mathrm{d}_2^{3/2}|\boldsymbol{g}|^{1/2})^{-1}$, $\tilde{\nu}_w = \nu_w(\rho_0 \mathrm{d}_2^{3/2}|\boldsymbol{g}|^{1/2})^{-1}$ with non-dimensionalized parameter $\mathrm{d}_2 = 0.005$ [78].

We set the initial conditions as $\boldsymbol{u}(0, \boldsymbol{x}) = (0, 0)^{\mathrm{t}}$, $\boldsymbol{m}(0, \boldsymbol{x}) = (0, 0)^{\mathrm{t}}$, $\boldsymbol{h}_a = (0, 0)^{\mathrm{t}}$, $p(0, \boldsymbol{x}) = 0$,

$$\Phi(0, \boldsymbol{x}) = \begin{cases} 0, & 0.5 + 0.5\tanh\frac{(x-0.5)^2+(y-0.5)^2-0.15^2}{2\sqrt{2}\varepsilon} \le 0.5, \\ 1, & \text{otherwise}, \end{cases} \tag{94}$$

the boundary conditions as

$$\partial_n \Phi|_{\partial\Omega} = 0, \ \partial_n W|_{\partial\Omega} = 0, \ \boldsymbol{u}|_{\partial\Omega} = \boldsymbol{0}, \ \partial_n \varphi|_{\partial\Omega} = (\boldsymbol{h}_a - \boldsymbol{m}) \cdot \boldsymbol{n}, \tag{95}$$

and the finite element spaces (34) with $l_1 = l_2 = l_3 = 2$. Based on [37,38,78], the physical parameters of the model (2.13) are opted as $\mathrm{d} = 1$, $\varepsilon = \lambda = 0.002$, $M = 0.0002$, $\rho_w = 1.161$, $\rho_f = 100\rho_w$, $\nu_w = 0.0000186$, $\rho_f = 0.0007977$, $\mu = 1$, $\tau = 0.0001$, $\chi_0 = 2$, $h = \frac{1}{64}$, $dt = 0.001$, $\epsilon = 0.01dt$.

To generate an approximate uniform applied magnetic field $\boldsymbol{h}_a$, we place five dipoles at a far end from the computational domain, and the positions $\boldsymbol{x}_s$ of dipoles are $(-0.5, -15)$, $(0, -15)$, $(0.5, -15)$, $(1, -15)$ and $(1.5, -15)$. The directions $\boldsymbol{d}$ of the five dipoles are $(0, 1)^{\mathrm{t}}$, and the intensity α_s is the same for the five dipoles and kept constant. This method is used to generate five uniform applied magnetic fields with magnetic strength $H_0 = 0.5$, 1, 2, 3 and 4, respectively.

In Fig. 1, we plot the time evolution of one circular ferrofluid droplet with $H_0 = 0.5$, 1, 2, 3 and 4. As can be seen from these figures, we observe that the circle ferrofluid droplet is elongated with time. The stronger the external magnetic field intensity H_0 is, the longer the ferrofluid droplet is stretched along the direction of the magnetic field under the equilibrium state, which is qualitatively consistent with the experimental results shown in [29,31,34]. In Fig. 2, we show the snapshots of the adaptive meshes corresponding to Fig. 1. Moreover, we plot the quantitative comparison between the analytical results (88) and the computed results in Fig. 3, and observe that the numerical results well agree with the analytical results.

5.3. An air bubble rising in oil based ferrofluid

The rising air bubble problem has been widely applied in the multiphase flow community to assess the space-time accuracy and robustness of methods [78,96–102]. The problem follows the trajectory of an air bubble submerged in a heavier fluid as it rises. The deformation of bubbles in ferrofluid can be traced back to the study in [103]. Then this issue was further studied in [22,104–106]. To provide a reference basis of the comparison purpose for the practical applications with high density and viscosity ratio, we simulate an air bubble rising in oil based ferrofluid in the following way. Assume the calculation domain $\Omega = (0, \mathrm{d}) \times (0, 1.5\mathrm{d})$ with initially

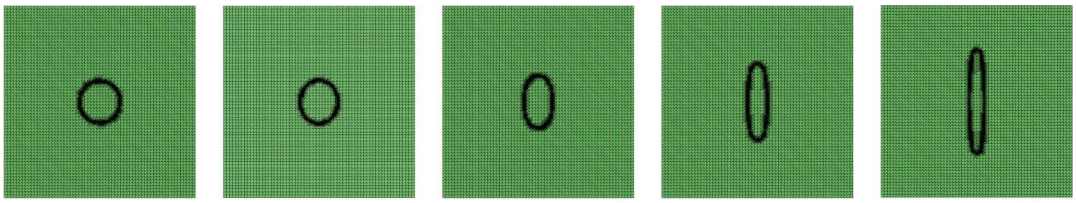

(a) H_0=0.5 (b) H_0=1 (c) H_0=2 (d) H_0=3 (e) H_0=4

Fig. 2. The adaptive meshes corresponding to Fig. 1, with $H_0 = 0.5$, 1, 2, 3 and 4.

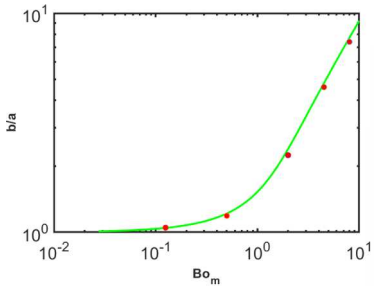

Fig. 3. Comparison between the analytical results and numerical results. Green solid line represents the analytical solution (88). Small red circles stand for the numerical results.

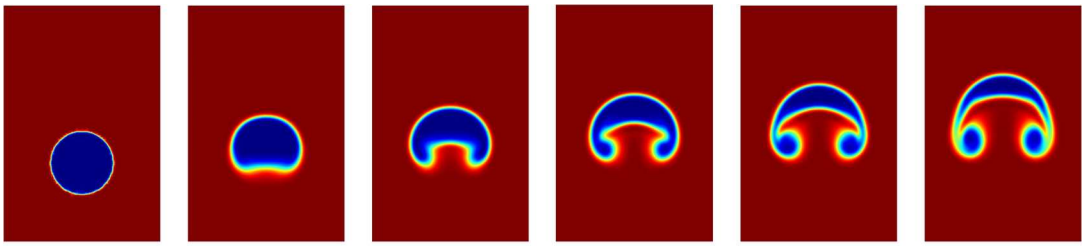

(a) t=0 (b) t=0.2 (c) t=0.3 (d) t=0.4 (e) t=0.5 (f) t=0.6

Fig. 4. Snapshots of the phase field variable Φ at $t = 0$, 0.2, 0.3, 0.4, 0.5 and 0.6.

air bubble of viscosity ν_w, density ρ_w in oil based ferrofluid of viscosity ν_f, density ρ_f. The gravity force as a forcing term $\rho\boldsymbol{g}$ is supplemented on the right-hand side of (13c). That is,

$$\sigma(\sigma\boldsymbol{u})_t + \frac{1}{2}\nabla\cdot(\rho\boldsymbol{u})\boldsymbol{u} + (\rho\boldsymbol{u}\cdot\nabla)\boldsymbol{u} - \nabla\cdot(\nu(\Phi)D(\boldsymbol{u})) + \nabla p + \frac{\lambda}{\epsilon}\Phi\nabla W = \mu(\boldsymbol{m}\cdot\nabla)\boldsymbol{h} + \rho\boldsymbol{g}. \tag{96}$$

We choose the initial condition as $\boldsymbol{u}(0,\boldsymbol{x}) = (0,0)^{\mathrm{t}}$, $\boldsymbol{m}(0,\boldsymbol{x}) = (0,0)^{\mathrm{t}}$, $\boldsymbol{h}_a = (0,0)^{\mathrm{t}}$, $p(0,\boldsymbol{x}) = 0$,

$$\Phi(0,\boldsymbol{x}) = \begin{cases} 0, & 0.5 + 0.5\tanh\frac{(x-0.5)^2+(y-0.5)^2-0.25^2}{2\sqrt{2}\epsilon} \le 0.5, \\ 1, & \text{otherwise}, \end{cases} \tag{97}$$

the boundary conditions as

$$\partial_n\Phi|_{\partial\Omega} = 0,\ \partial_n W|_{\partial\Omega} = 0,\ \boldsymbol{u}|_{\partial\Omega} = \boldsymbol{0},\ \partial_n\varphi|_{\partial\Omega} = (\boldsymbol{h}_a - \boldsymbol{m})\cdot\boldsymbol{n}, \tag{98}$$

and the finite element spaces (34) with $l_1 = l_2 = l_3 = 2$. Based on [37,99], the physical parameters are chosen as

$$\begin{cases} \epsilon = \lambda = 0.01,\ M = 0.00004,\ \mathrm{d} = 1,\ \mu = 1,\ \tau = 0.0001,\ \chi_0 = 2,\ h = \frac{1}{32},\ dt = 0.001, \\ \epsilon = 0.01dt,\ \rho_w = 1.161,\ \rho_f = 100\rho_w,\ \nu_f = 0.0007977,\ \nu_w = 0.0000186,\ \boldsymbol{g} = (0,-10)^{\mathrm{t}}. \end{cases} \tag{99}$$

In Fig. 4, we plot the snapshots of an air bubble rising in oil based ferrofluid without uniformly applied magnetic field $\boldsymbol{h}_a$ at $t = 0$, 0.2, 0.3, 0.4, 0.5 and 0.6. The low density bubble keeps rising and has obvious deformation, and we observe two counter-rotating vortices at the tail of the bubble. This simulation result is expected based on the experimental results of a bubble rising in ferrofluid [107–109]. In Fig. 5, we show the snapshots of the adaptive meshes corresponding to Fig. 4.

Because ferrofluid can be controlled by applying a magnetic field, we simulate the dynamic behavior of a bubble rising in oil based ferrofluid under a uniform magnetic field. Similar to the a ferrofluid droplet deformation experiment, we place five dipoles at

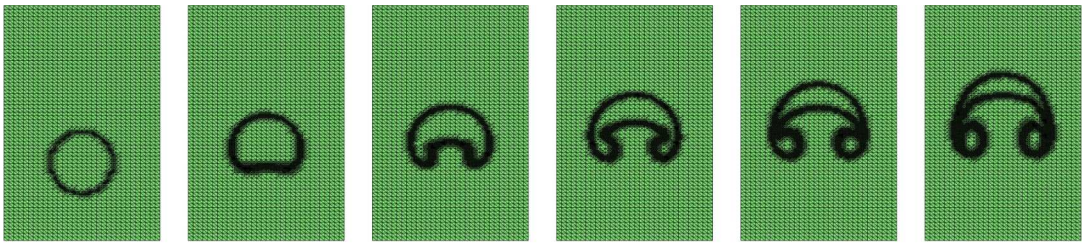

Fig. 5. The adaptive meshes corresponding to Fig. 4, at $t = 0$, 0.2, 0.3, 0.4, 0.5 and 0.6.

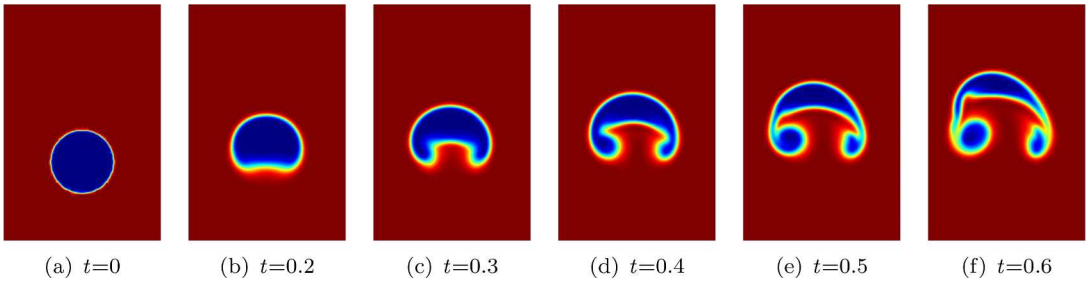

Fig. 6. Snapshots of the phase field variable Φ at $t = 0$, 0.2, 0.3, 0.4, 0.5 and 0.6.

$(-0.5, -15)$, $(0, -15)$, $(0.5, -15)$, $(1, -15)$ and $(1.5, -15)$ to generate an approximate uniform applied magnetic field $\boldsymbol{h}_a$. The intensity α_s is the same for the five dipoles but increases linearly in time with a slope of 3000, starting from $\alpha_s = 0$ at time $t = 0$ to maximum value $\alpha_s = 1800$ at time $t = 0.6$. From $t = 0.6$ the intensity is kept constant. The direction of the five dipoles are the same.

In Fig. 6, we summarize the time evolution of an air bubble droplets under uniformly applied magnetic field $\boldsymbol{h}_a$ by generating $\boldsymbol{d} = (\frac{\sqrt{2}}{2}, \frac{\sqrt{2}}{2})^{\mathrm{t}}$. We observe that these pictures are obviously different from the corresponding pictures in Fig. 4, especially at $t = 0.4$, 0.5 and 0.6. From the top to the bottom in Fig. 7, we show the velocity, pressure, magnetic field and effective magnetic field diagrams corresponding to Fig. 6. We observe that these pictures are not symmetrical and the bubble deforms along the magnetic field direction, which is caused by the direction of applied magnetic field $\boldsymbol{d} = (\frac{\sqrt{2}}{2}, \frac{\sqrt{2}}{2})^{\mathrm{t}}$. This simulation result is qualitatively consistent with the experimental observations and the corresponding explanations for the bubble rising in ferrofluid in [109].

5.4. Two air bubbles rising in oil based ferrofluid

In this section, we simulate two air bubbles rising in oil based ferrofluid by using the proposed algorithm. The problem domain, finite element spaces, initial conditions, boundary conditions and model parameters are still the same as those of the air bubble in the previous section, but

$$\Phi(0, \boldsymbol{x}) = \begin{cases} 0, & (0.5 + 0.5\tanh\frac{(x-0.5)^2+(y-0.3)^2-0.15^2}{0.004\sqrt{2}})(0.5 + 0.5\tanh\frac{(x-0.5)^2+(y-0.7)^2-0.15^2}{0.004\sqrt{2}}) \leq 0.5, \\ 1, & \text{otherwise.} \end{cases} \tag{100}$$

Fig. 8 depicts the snapshots of two air bubbles rising in oil based ferrofluid without uniformly applied magnetic field $\boldsymbol{h}_a$ at $t = 0$, 0.4, 0.5, 0.8, 0.9 and 1. We observe that the bubble below rises faster and the deformation of the two bubbles is obviously different. The deformation of each bubble in this experiment is different from that of the bubble in the previous section, due to the two bubbles' influence on each other. After the two bubbles start to merge together, their deformation becomes even more complicated and continues to rise. In Fig. 9, we show the snapshots of the adaptive meshes corresponding to Fig. 8.

Next, we simulate the time evolution of two air bubbles droplets under uniformly applied magnetic field $\boldsymbol{h}_a$ by generating $\boldsymbol{d} = (-\frac{\sqrt{2}}{2}, \frac{\sqrt{2}}{2})^{\mathrm{t}}$ in Fig. 10. We clearly observe that the bubbles deform along the magnetic field direction, which is expected theoretically.

5.5. An oil based ferrofluid droplet as controllable liquid microrobot

In recent years, the development of magnetically controlled microrobots has received more attention and experienced significant progress [110–113]. These minuscule robotic systems possess distinctive capabilities that enable them to access confined spaces and execute intricate tasks with minimal disruption to their surrounding environments. Compared with light field drive [114] and electric field drive [115], magnetically controlled microrobots stand out due to their inherent advantages, such as wireless actuation, non-invasive control, reduced size and complexity, and improved adaptability. Since ferrofluid can be controlled by an external magnetic

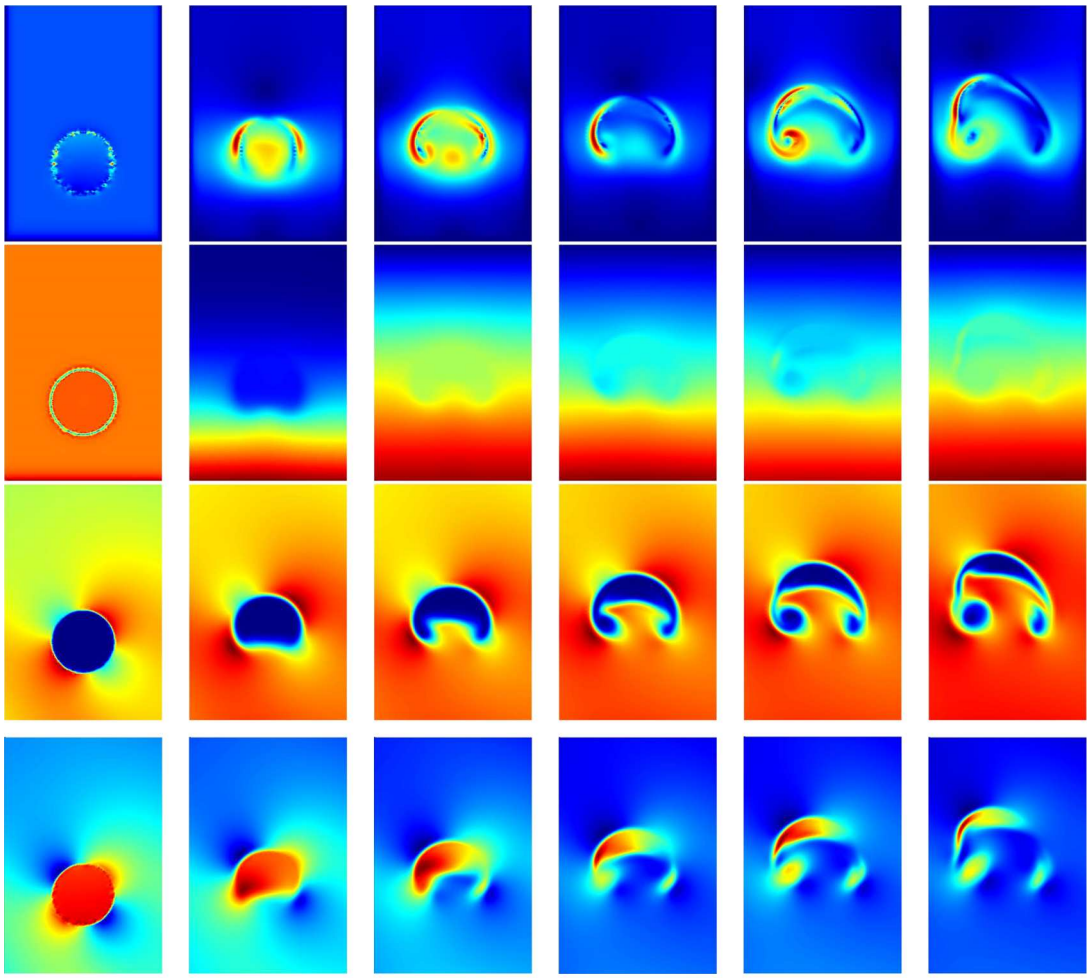

Fig. 7. From top to bottom, the velocity, pressure, magnetizing field, effective magnetizing field corresponding to Fig. 6.

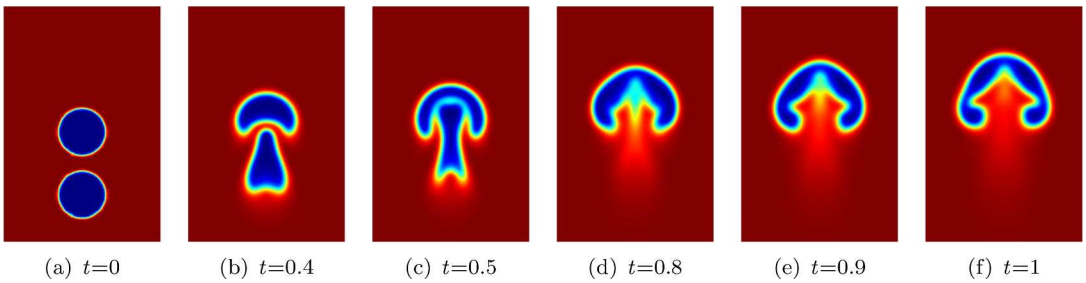

Fig. 8. Snapshots of the phase field variable Φ at t = 0, 0.4, 0.5, 0.8, 0.9 and 1.

field, ferrofluid microrobots have very promising potential in various fields, hence have received more and more attentions [116–118]. Moreover, Y-shaped computing region is used to separate ferrofluid droplets from water droplets in [119] and control the formation of ferrofluid droplets in focused microchannels [120].

In this section, we simulate for the Y-shaped computing area and control the movement of the oil based ferrofluid droplet microrobot by applying an external magnetic field. To do so, we use the same finite element spaces, initial conditions, boundary conditions

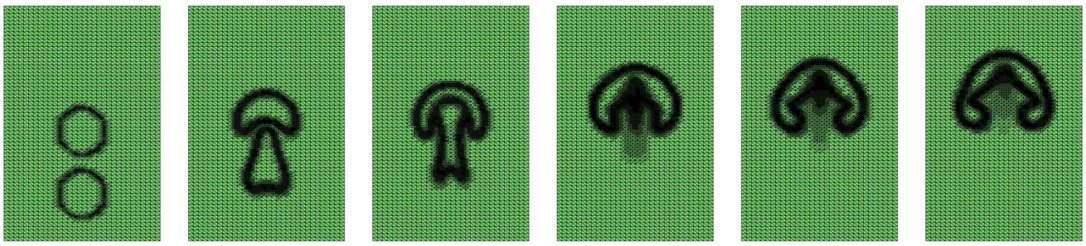

Fig. 9. The adaptive meshes corresponding to Fig. 8, at $t = 0, 0.4, 0.5, 0.8, 0.9$ and 1.

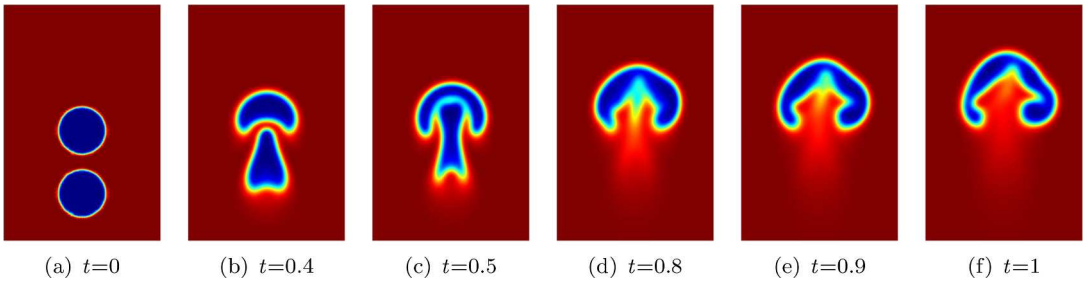

Fig. 10. Snapshots of the phase field variable Φ at $t = 0, 0.4, 0.5, 0.8, 0.9$ and 1.

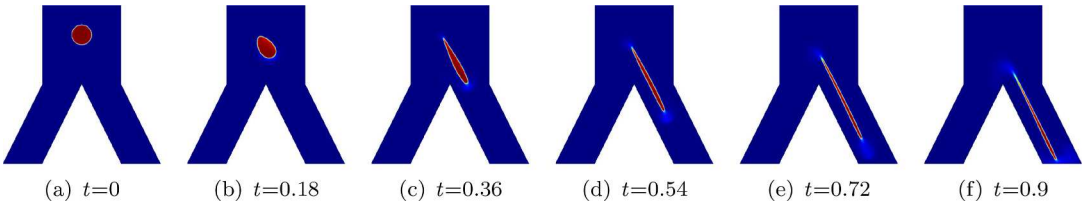

Fig. 11. Snapshots of the phase field variable Φ at $t = 0, 0.18, 0.36, 0.54, 0.72$ and 0.9.

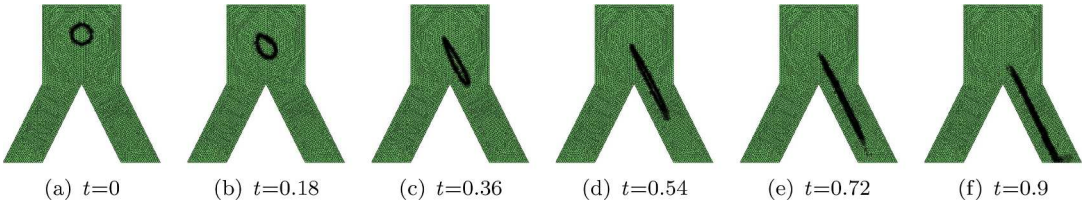

Fig. 12. The adaptive meshes corresponding to Fig. 11, at $t = 0, 0.18, 0.36, 0.54, 0.72$ and 0.9.

and physical parameters as in Section 5.3 but with $\varepsilon = \lambda = 0.001$, $\chi_0 = 0.5$, $M = 0.000004$ and

$$\Phi(0, \boldsymbol{x}) = \begin{cases} 1, & 0.5 + 0.5\tanh\frac{(x-0.4)^2+(y-0.65)^2-0.05^2}{2\sqrt{2}\varepsilon} \le 0.5, \\ 0, & \text{otherwise}. \end{cases} \tag{101}$$

Furthermore, we place five dipoles at $(-0.5, -15)$, $(0, -15)$, $(0.5, -15)$, $(1, -15)$ and $(1.5, -15)$ to generate an approximate uniform applied magnetic field $\boldsymbol{h}_a$. The intensity α_s is the same for the five dipoles but increases linearly in time with a slope of 10000, starting from $\alpha_s = 0$ at time $t = 0$ to maximum value $\alpha_s = 9000$ at time $t = 0.9$. From $t = 0.9$ the intensity is kept constant. The direction of the five dipoles are the same.

In Figs. 11 and 13, we show the time evolution of oil based ferrofluid droplet under uniformly magnetic field $\boldsymbol{h}_a$ by generating $\boldsymbol{d} = (-\frac{\sqrt{5}}{5}, -\frac{2\sqrt{5}}{5})^t$ and $\boldsymbol{d} = (\frac{\sqrt{5}}{5}, -\frac{2\sqrt{5}}{5})^t$, respectively. These experimental results show that the moving direction of ferrofluid droplets can be well controlled by the direction of applied magnetic field. Moreover, the snapshots of the adaptive meshes corresponding to Fig. 11 are shown in Fig. 12.

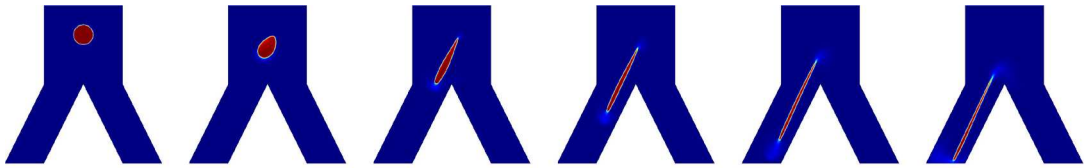

Fig. 13. Snapshots of the phase field variable Φ at $t = 0$, 0.18, 0.36, 0.54, 0.72 and 0.9.

5.6. Rosensweig instability under uniformly applied magnetic field

In this part, we simulate a benchmark problem, the so-called Rosensweig instability [31,32,36–38,121], under uniformly applied magnetic field. The uniformly applied magnetic field $\boldsymbol{h}_a$ in (90) is generated by 5 dipoles with far distance from the computational domain: $(-0.5, -15)$, $(0, -15)$, $(0.5, -15)$, $(1, -15)$ and $(1.5, -15)$. The direction of the 5 dipoles are the same and $\boldsymbol{d} = (0, 1)^{\mathrm{t}}$. The intensity α_s is the same for the 5 dipoles but increases linearly in time with a slope of 25000, starting from $\alpha_s = 0$ at time $t = 0$ to the maximum value $\alpha_s = 5000$ at time $t = 0.2$, and from $t = 0.2$ the intensity is kept constant.

In order to simulate a mixture of air and oil based ferrofluid under uniformly applied magnetic field, we choose the calculation domain $\Omega = (0, \mathrm{d}) \times (0, 0.6\mathrm{d})$, the finite element space (34) with $l_1 = l_2 = l_3 = 2$, the initial condition as $\boldsymbol{u}(0, \boldsymbol{x}) = (0, 0)^{\mathrm{t}}$, $\boldsymbol{m}(0, \boldsymbol{x}) = (0, 0)^{\mathrm{t}}$, $p(0, \boldsymbol{x}) = 0$, $\boldsymbol{h}_a = (0, 0)^{\mathrm{t}}$,

$$\Phi(0, \boldsymbol{x}) = 0.5 - 0.5\tanh\left(\frac{|y| - 0.2}{2\sqrt{2}\epsilon}\right), \tag{102}$$

and the boundary conditions as

$$\partial_n \Phi|_{\partial\Omega} = 0,\ \partial_n W|_{\partial\Omega} = 0,\ \boldsymbol{u}|_{\partial\Omega} = \boldsymbol{0},\ \partial_n \varphi|_{\partial\Omega} = (\boldsymbol{h}_a - \boldsymbol{m}) \cdot \boldsymbol{n}. \tag{103}$$

Similar to the bubble rising experiment, we supplement the gravity force as a forcing term $\rho \boldsymbol{g}$ on the right-hand side of (13c). Based on [37,38], the model parameters are chosen as

$$\begin{cases} \epsilon = \lambda = 0.005,\ M = 0.0005,\ \mathrm{d} = 1,\ \mu = 1,\ \tau = 0.00001,\ \chi_0 = 0.5,\ h = \frac{1}{80},\ dt = 0.001, \\ \epsilon = 0.01dt,\ \boldsymbol{g} = (0, -10)^{\mathrm{t}},\ \rho_w = 1.161,\ \rho_f = 600\rho_w,\ \nu_f = 0.0026,\ \nu_w = 0.0013. \end{cases} \tag{104}$$

In Fig. 14, we show the snapshots of the phase variable Φ. We observe that six spikes gradually appear and the directions of the "sawtooth" are aligned with the applied uniform magnetic field. In Fig. 15, we show the adaptive mesh diagrams corresponding to Fig. 14. From left to right in Fig. 16, snapshots of the velocity field $\boldsymbol{u}$, the pressure p, the magnetization field $\boldsymbol{m}$ and the effective magnetizing field $\boldsymbol{h}$ are shown at $t = 2.5$ of corresponding to Fig. 14. These results are consistent with the experimental results shown in [37–39].

5.7. Rosensweig instability under nonuniformly applied magnetic field

To validate the developed model (2.13) and show the robustness of our scheme (38)–(46), we simulate a benchmark simulation by the so-called Rosensweig instability [32,37–39,122] under nonuniformly applied magnetic field. That is, we consider a mixture of air and oil based ferrofluid under nonuniformly applied magnetic field. The nonuniformly applied magnetic field $\boldsymbol{h}_a$ in (90) is generated by 42 dipoles. The dipoles are placed in three rows, that is, $y = -0.5$, $y = -0.75$, and $y = -1$, the 14 dipoles pointing upwards $\boldsymbol{d} = (0, 1)^{\mathrm{t}}$

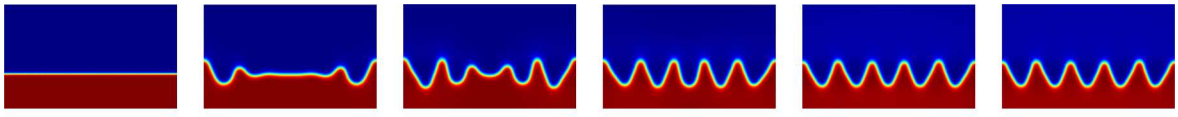

Fig. 14. Snapshots of the phase field variable Φ at $t = 0$, 0.6, 0.8, 1, 2 and 2.5.

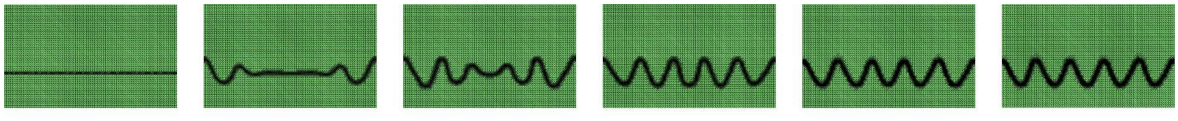

Fig. 15. The adaptive meshes corresponding to Fig. 14, $t = 0$, 0.6, 0.8, 1, 2 and 2.5.

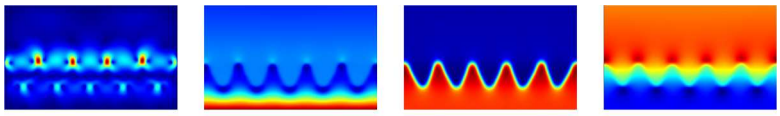

(a) $\boldsymbol{u}$ (b) p (c) $\boldsymbol{m}$ (d) $\boldsymbol{h}$

Fig. 16. Snapshots of the velocity field $\boldsymbol{u}$, the pressure p, the magnetization field $\boldsymbol{m}$ and the effective magnetizing field $\boldsymbol{h}$ at $t = 2.5$.

in each row are equidistributed in the x direction. The intention of this setup of the dipoles is to create a crude approximation of a bar magnet of 0.4 units width and 0.5 units height. The intensity α_s is the same for each dipole but increases linearly in time with a slope of 3.

We use the control variable method to explore the influence of density and viscosity on Rosenweig instability. More specifically, keeping the viscosity and density of air constant, we fix the density of oil based ferrofluid to explore the influence of viscosity on Rosenweig instability, or fix the viscosity of oil based ferrofluid to explore the influence of density on Rosenweig instability. Similar to the bubble rising experiment, we supplement the gravity force as a forcing term $\rho\boldsymbol{g}$ on the right-hand side of (13c). Moreover, we choose the same problem domain, finite element spaces, initial conditions and boundary conditions as in Section 5.6, except

$$\Phi(0,\boldsymbol{x}) = 0.5 - 0.5\tanh\left(\frac{|y| - 0.1}{2\sqrt{2}\epsilon}\right). \tag{105}$$

Based on [37,99], the model parameters are chosen as

$$\begin{cases} \epsilon = 0.001,\ \lambda = 0.005,\ \boldsymbol{M} = 0.0002,\ \mathrm{d} = 1,\ \tau = 0.0001,\ \chi_0 = 0.9,\ h = \frac{1}{80}, \\ dt = 0.001,\ \epsilon = 0.01dt,\ \boldsymbol{g} = (0,-10)^{\mathrm{t}},\ \rho_w = 1.161,\ \nu_w = 0.0000186. \end{cases} \tag{106}$$

Firstly, we fix the viscosity of oil based ferrofluid as $\nu_f = 0.0007977$ to explore the influence of density on Rosenweig instability. To this end, we design numerical simulations from a low density ratio of 1:100 to a high density ratio of 1:900. For the comparison, we show three simulation results. In Figs. 17, 19, and 20, we draw the snapshots of the phase variables Φ with density ratios of air to oil based ferrofluid of 1:100, 1:500 and 1:900 at six different times, respectively. From these simulation results, we observe that the greater the density of oil based ferrofluid, the slower the occurrence of Rosenweig instability and the lower the spikes formed by Rosenweig instability. Furthermore, the snapshots of the adaptive meshes corresponding to Fig. 17 are shown in Fig. 18.

Next, we fix the density of oil based ferrofluid as $\rho_f = 1050$ to explore the influence of viscosity on Rosenweig instability. For this propose, we design viscosity ratio numerical simulations from 1:100 to 1:500. For the comparison purpose, we show three simulation results. In Figs. 21–23, we draw the snapshots of the phase variables Φ with viscosity ratios of air to oil based ferrofluid of 1:100, 1:200 and 1:500 at $t = 0$, 0.8, 1, 1.2, 1.5, 2, respectively. From the pictures of three experiments at $t = 1$, and 1.2, we observe that the greater the viscosity of oil based ferrofluids, the slower the Rosenweig instability occurs. From the top to the bottom in Fig. 24, we show the velocity, pressure, magnetic field, and effective magnetic field corresponding to Fig. 23.

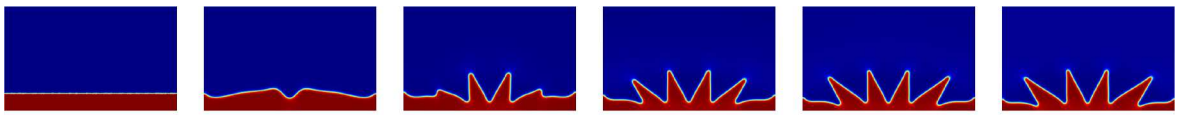

(a) t=0 (b) t=0.5 (c) t=0.7 (d) t=0.9 (e) t=1.2 (f) t=2

Fig. 17. Snapshots of the phase field variable Φ at six different times with $\rho_w : \rho_f = 1 : 100$.

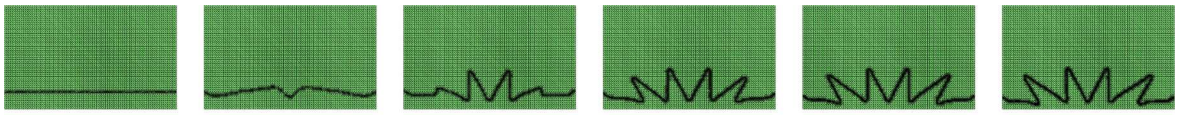

(a) t=0 (b) t=0.5 (c) t=0.7 (d) t=0.9 (e) t=1.2 (f) t=2

Fig. 18. The adaptive meshes corresponding to Fig. 17, at $t = 0$, 0.5, 0.7, 0.9, 1.2 and 2.

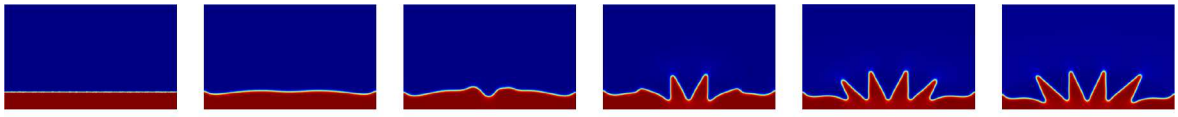

(a) t=0 (b) t=0.5 (c) t=0.7 (d) t=0.9 (e) t=1.2 (f) t=2

Fig. 19. Snapshots of the phase field variable Φ at six different times with $\rho_w : \rho_f = 1 : 500$.

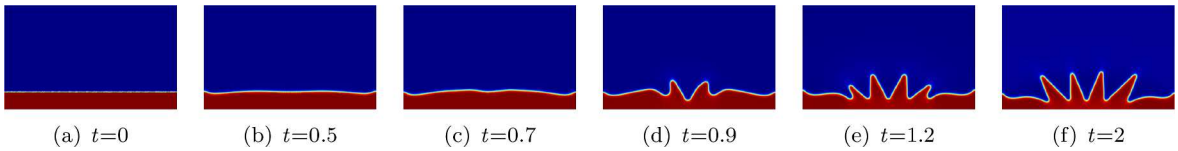

Fig. 20. Snapshots of the phase field variable Φ at six different times with $\rho_w : \rho_f = 1 : 900$.

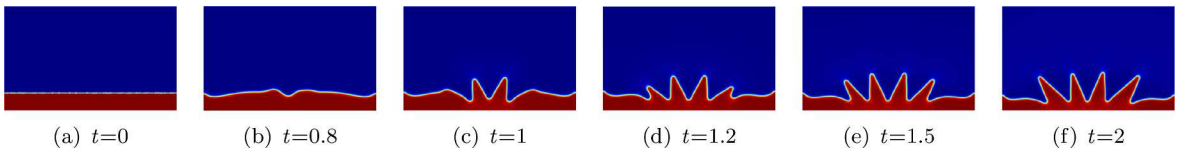

Fig. 21. Snapshots of the phase field variable Φ at six different times with $\nu_w : \nu_f = 1 : 100$.

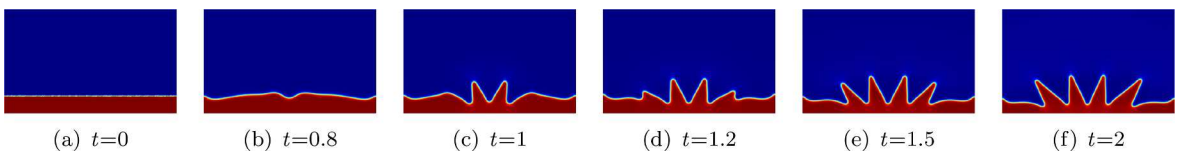

Fig. 22. Snapshots of the phase field variable Φ at six different times with $\nu_w : \nu_f = 1 : 200$.

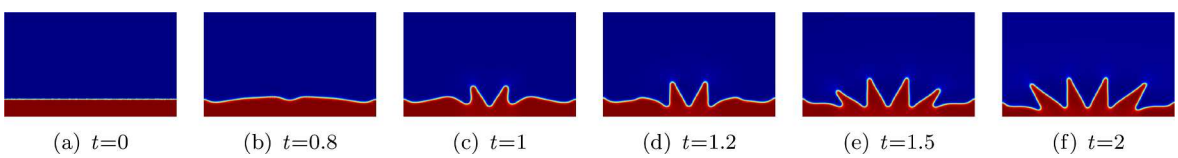

Fig. 23. Snapshots of the phase field variable Φ at six different times with $\nu_w : \nu_f = 1 : 500$.

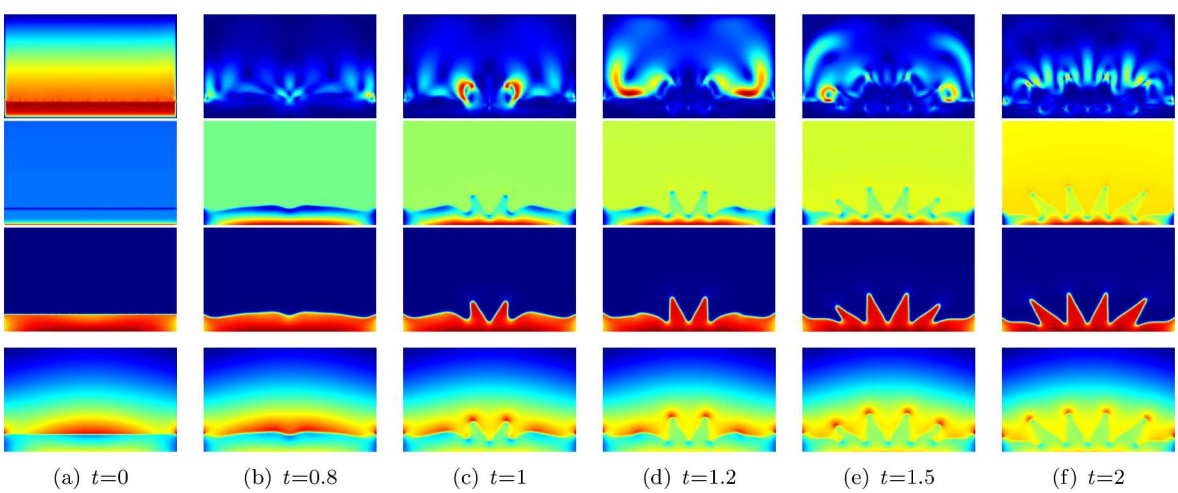

Fig. 24. From top to bottom, the velocity, pressure, magnetizing field, and effective magnetizing field corresponding to Fig. 23.

The above simulation results are qualitatively consistent with the experimental results shown in [37–39]. These results validate the two-phase ferrofluids with different densities and viscosities and the finite element scheme proposed in this paper. Up to the authors' knowledge, this is the first phase field work to explore the influence of different densities and viscosities of ferrofluid on Rosenweig instability.

6. Conclusions

In this paper, we propose a diffuse interface model describing the behavior of two-phase ferrofluid flows with different densities and viscosities. This model is the highly nonlinear and coupled multiphysics PDE system consisting of Cahn-Hilliard equations, Navier-

Stokes equations, magnetization equation and magnetostatic equation. Then we propose a linear, decoupled, unconditionally stable, and fully discrete finite element method to solve this model. In order to accurately capture the diffuse interface in the numerical simulation, we also apply the adaptive mesh strategy to locally refine the mesh around the interfacial region. Finally, we perform several informative numerical experiments to illustrate various features of the proposed model and scheme.

CRediT authorship contribution statement

Xiaoyong Chen: Writing – original draft, Methodology, Validation, Formal analysis, Software, Conceptualization; **Rui Li:** Validation, Resources, Funding acquisition, Supervision, Project administration, Formal analysis, Writing – review & editing, Software, Methodology, Conceptualization; **Jian Li:** Writing – review & editing, Project administration, Formal analysis, Supervision, Methodology, Conceptualization, Resources, Funding acquisition; **Xiaoming He:** Validation, Methodology, Writing – review & editing, Formal analysis.

Data availability

Data will be made available on request.

Declaration of competing interest

The authors declare that they have no known competing financial interests or personal relationships that could have appeared to influence the work reported in this paper. Xiaoyong Chen, Rui Li, Jian Li, Xiaoming He.

Acknowledgement

The second author is supported by the National Natural Science Foundation of China Nos. (12371406, 11901372) and the Natural Science Foundation of Shaanxi Province No. (2024JC-YBMS-063). The third author is supported in part by National Natural Science Foundation of China Nos. (12431016, 12471408). The fourth author is supported by NSF No. (DMS-2309733).

References

[1] Y. Amirat, K. Hamdache, F. Murat, Global weak solutions to equations of motion for magnetic fluids, J. Math. Fluid Mech. 10 (2008) 326–351.
[2] F. Bai, D.Z. Han, X.M. He, X.F. Yang, Deformation and coalescence of ferrodroplets in Rosensweig model using the phase field and modified level set approaches under uniform magnetic fields, Commun. Nonlinear Sci. Numer. Simul. 85 (2020) 105213.
[3] C. Rinaldi, M. Zahn, Effects of spin viscosity on ferrofluid flow profiles in alternating and rotating magnetic fields, Phys. Fluids. 14 (2002) 2847–2870.
[4] A. Chaves, C. Rinaldi, Interfacial stress balances in structured continua and free surface flows in ferrofluids, Phys. Fluids. 26 (2014) 042101.
[5] R.E. Rosensweig, Magnetic fluids, Ann. Rev. Fluid Mech. 19 (1987) 437–461.
[6] S. Venkatasubramanian, P.N. Kaloni, Stability and uniqueness of magnetic fluid motions, Proc. Math. Phys. Eng. Sci. 458 (2002) 1189–1204.
[7] G. Zhang, X.-M. He, X. Yang, Efficient fully-discrete finite element scheme for the ferrohydrodynamic Rosensweig model and simulations of ferrofluid rotational flow problems, SIAM J. Sci. Comput. 47 (2025) B28–B58.
[8] Y. Amirat, K. Hamdache, Strong solutions to the equations of a ferrofluid flow model, J. Math. Anal. Appl. 353 (2009) 271–294.
[9] M.I. Shliomis, Effective viscosity of magnetic suspensions, Sov. Phys. Jetp. 34 (1972) 1291–1294.
[10] M.I. Shliomis, Ferrohydrodynamics: retrospective and issues, Lect. Notes Phys. 594 (2002) 85–111.
[11] M. Sheikholeslami, D.D. Ganji, Ferrohydrodynamic and magnetohydrodynamic effects on ferrofluid flow and convective heat transfer, Energy 75 (2014) 400–410.
[12] J. Wang, G.L. Li, H.X. Zhu, J. Luo, B. Sundén, Experimental investigation on convective heat transfer of ferrofluids inside a pipe under various magnet orientations, Int. J. Heat. Mass Tranf. 132 (2019) 407–419.
[13] M. Miwa, H. Harita, T. Nishigami, R. Kaneko, H. Unozawa, Frequency characteristics of stiffness and damping effect of a ferrofluid bearing, Tribol. Lett. 15 (2003) 97–105.
[14] K. Raj, B. Moskowitz, R. Casciari, Advances in ferrofluid technology, J. Magn. Magn. Mater. 149 (1995) 174–180.
[15] F. Bai, X.-M. He, R. Zhou, X. Yang, C. Wang, Three dimensional phase-field investigation of droplet formation in microfluidic flow focusing devices with experimental validation, Int. J. Multiphase Flow 93 (2017) 130–141.
[16] I. Torres-Diaz, C. Rinaldi, Recent progress in ferrofluids research: novel applications of magnetically controllable and tunable fluids, Soft Matter 10 (2014) 8584–8602.
[17] M. Kole, S. Khandekar, Engineering applications of ferrofluids: A review, J. Magn. Magn. Mater. 537 (2021) 168222.
[18] M. Latorre-Esteves, C. Rinaldi, Applications of magnetic nanoparticles in medicine: magnetic fluid hyperthermia, PR Health Sci. J. 28 (2009) 227–238.
[19] Q.A. Pankhurst, J. Connolly, S.K. Jones, J. Dobson, Applications of magnetic nanoparticles in biomedicine, J. Phys. D Appl. Phys. 36 (2003) R167–R181.
[20] A. Sarwar, R. Lee, D.A. Depireux, B. Shapiro, Magnetic injection of nanoparticles into rat inner ears at a human head working distance, IEEE Trans. Maga. 49 (2013) 440–452.
[21] D.X. Shi, Q.C. Bi, R.Q. Zhou, Numerical simulation of a falling ferrofluid droplet in a uniform magnetic field by the VOSET method, Numer. Heat. Transf. A-Appl. 66 (2014) 144–164.
[22] S. Afkhami, Y. Renardy, M. Renardy, J.S. Riffle, T.S. Pierre, Field-induced motion of ferrofluid droplets through immiscible viscous media, J. Fluid Mech. 610 (2008) 363–380.
[23] S. Afkhami, A.J. Tyler, Y. Renardy, M. Renardy, T.G.S. Pierre, R.C. Woodward, J.S. Riffle, Deformation of a hydrophobic ferrofluid droplet suspended in a viscous medium under uniform magnetic fields, J. Fluid Mech. 663 (2010) 358–384.
[24] M. Habera, J. Hron, Modelling of a free-surface ferrofluid flow, J. Magn. Magn. Mater. 431 (2017) 157–160.
[25] L.H.P. Cunha, I.R. Siqueira, F.R. Cunha, T.F. Oliveira, Effects of external magnetic fields on the rheology and magnetization of dilute emulsions of ferrofluid droplets in shear flows, Phys. Fluids. 32 (2020) 073306.
[26] T. Tagawa, Numerical simulation of two-phase flows in the presence of a magnetic field, Math. Comput. Simul. 72 (2006) 212–219.
[27] H. Ki, Level set method for two-phase incompressible flows under magnetic fields, Comput. Phys. Commun. 181 (2010) 999–1007.

[28] A. Ghaffari, S.H. Hashemabadi, M. Bazmi, CFD simulation of equilibrium shape and coalescence of ferrofluid droplets subjected to uniform magnetic field, Colloids Surf. A Physicochem. Eng. Asp. 481 (2015) 186–198.
[29] Y. Hu, D.C. Li, X.D. Niu, Phase-field-based lattice Boltzmann model for multiphase ferrofluid flows, Phys. Rev. E 98 (2018) 033301.
[30] Y. Hu, D.C. Li, X.D. Niu, S. Shu, A diffuse interface lattice Boltzmann model for thermocapillary flows with large density ratio and thermophysical parameters contrasts, Int. J. Heat Mass Transf. 138 (2019) 809–824.
[31] X. Li, Z.Q. Dong, L.P. Wang, X.D. Niu, H. Yamaguchi, D.C. Li, P. Yu, A magnetic field coupling fractional step lattice Boltamann model for the complex interfacial behavior in magnetic multiphase flows, Appl. Math. Model. 117 (2023) 219–250.
[32] X.D. Niu, A. Khan, Y. Ouyang, M.F. Chen, D.C. Li, H. Yamaguchi, A simplified phase-field lattice Boltzmann method with a self-corrected magnetic field for the evolution of spike structures in ferrofluids, Appl. Math. Comput. 436 (2023) 127503.
[33] Q.Z. Li, Z.L. Lu, D. Zhou, X.D. Niu, T.Q. Guo, B.C. Du, Unified simplified multiphase lattice Boltzmann method for ferrofluid flows and its application, Phys. Fluids. 32 (2020) 093302.
[34] A. Khan, X.D. Niu, Q.Z. Li, Y. Li, D. Li, H. Yamaguchi, Dynamic study of ferrodroplet and bubbles merging in ferrofluid by a simplified multiphase lattice Boltzmann method, J. Magn. Magn. Mater. 495 (2020) 165869.
[35] Y. Hu, D.C. Li, Q. He, Generalized conservative phase field model and its lattice Boltzmann scheme for multicomponent multiphase flows, Int. J. Multiphase Flow 132 (2020) 103432.
[36] X.F. Li, Y.P. Wang, Y.C. Zhang, T.P. He, X.D. Niu, A. Khan, D.C. Li, H. Yamaguchi, On the Rosensweig instability of ferrofluid-infused surfaces under a uniform magnetic field, Phys. Fluids. 35 (2023) 113306.
[37] R.H. Nochetto, A.J. Salgado, I. Tomas, A diffuse interface model for two-phase ferrofluid flows, Comput. Methods Appl. Mech. Eng. 309 (2016) 497–531.
[38] G.D. Zhang, X.M. He, X.F. Yang, Decoupled, linear, and unconditionally energy stable fully discrete finite element numerical scheme for a two-phase ferrohydrodynamics model, SIAM J. Sci. Comput. 43 (2021) B167–B193.
[39] G.D. Zhang, X.M. He, X.F. Yang, Reformulated weak formulation and efficient fully discrete finite element method for a two-phase ferrohydrodynamics Shliomis model, SIAM J. Sci. Comput. 45 (2023) B253–B282.
[40] G. Zhang, X.-M. He, X. Yang, A unified framework of the SAV-ZEC method for a mass-conserved Allen-Cahn type two-phase ferrofluid flow model, SIAM J. Sci. Comput. 46 (2) (2024) B77–B106.
[41] Z. Guan, C. Wang, S.W. Wise, A convergent convex splitting scheme for the periodic nonlocal Cahn-Hilliard equation, Numer. Math. 128 (2014) 377–406.
[42] H. Gomez, T.J.R. Hughes, Provably unconditionally stable, second-order time-accurate, mixed variational methods for phase-field models, J. Comput. Phys. 230 (2011) 5310–5327.
[43] J. Li, J.Y. Zeng, R. Li, An adaptive discontinuous finite volume element method for the Allen-Cahn equation, Adv. Comput. Math. 49 (2023) 55.
[44] R. Li, Y.L. Gao, J. Chen, L. Zhang, X.M. He, Z.X. Chen, Discontinuous finite volume element method for a coupled Navier-Stokes-Cahn-Hilliard phase field model, Adv. Comput. Math. 46 (2020) 25.
[45] X.Y. Feng, Z.H. Qiao, S.Y. Sun, X.P. Wang, An energy-stable smoothed particle hydrodynamics discretization of the Navier-Stokes-Cahn-Hilliard model for incompressible two-phase flows, J. Comput. Phys. 479 (2023) 111997.
[46] Y.Y. Cai, H. Choi, J. Shen, Error estimates for time discretizations of Cahn-Hilliard and Allen-Cahn phase-field models for two-phase incompressible flows, Numer. Math. 137 (2017) 417–449.
[47] Q. Huang, X. Yang, X.M. He, Numerical approximations for a smectic-A liquid crystal flow model: first-order, linear, decoupled and energy stable schemes, Discrete Contin. Dyn. Syst. Ser. B 23 (6) (2018) 2177–2192.
[48] C.J. Xu, T. Tang, Stability analysis of large time-stepping methods for epitaxial growth models, SIAM J. Numer. Anal. 44 (2006) 1759–1779.
[49] X.L. Feng, T. Tang, J. Yang, Stabilized Crank-Nicolson/Adams-Bashforth schemes for phase field models, East Asian J. Appl. Math. 3 (2013) 59–80.
[50] C.J. Chen, X.F. Yang, Fully-discrete finite element numerical scheme with decoupling structure and energy stability for the Cahn-Hilliard phase-field model of two-phase incompressible flow system with variable density and viscosity, ESAIM Math. Model. Numer. Anal. 55 (2021) 2323–2347.
[51] J.S. Kou, X.H. Wang, S.G. Du, S.Y. Sun, An energy stable linear numerical method for thermodynamically consistent modeling of two-phase incompressible flow in porous media, J. Comput. Phys. 451 (2022) 110854.
[52] X.F. Yang, J. Zhao, Q. Wang, J. Shen, Numerical approximations for a three component Cahn-Hilliard phase-field model based on the invariant energy quadratization method, Math. Models Methods Appl. Sci. 27 (2017) 1993–2030.
[53] J. Zhao, Q. Wang, X.F. Yang, Numerical approximations for a phase field dendritic crystal growth model based on the invariant energy quadratization approach, Inter. J. Num. Meth. Eng. 110 (2017) 279–300.
[54] Q. Cheng, X.F. Yang, J. Shen, Efficient and accurate numerical schemes for a hydrodynamically coupled phase field diblock copolymer model, J. Comput. Phys. 341 (2017) 44–60.
[55] X. Yang, J. Zhao, X.M. He, Linear, second order and unconditionally energy stable schemes for the viscous Cahn-Hilliard equation with hyperbolic relaxation using the invariant energy quadratization method, J. Comput. Appl. Math. 343 (1) (2018) 80–97.
[56] C. Xu, C. Chen, X. Yang, X.M. He, Numerical approximations for the hydrodynamics coupled binary surfactant phase field model: second order, linear, unconditionally energy stable schemes, Commun. Math. Sci. 17 (2019) 835–858.
[57] Z.H. Qiao, S.Y. Sun, T. Zhang, Y.Z. Zhang, A new multi-component diffuse interface model with Peng-Robinson equation of state and its scalar auxiliary variable (SAV) approach, Commun. Comput. Phys. 26 (2019) 1597–1616.
[58] J. Shen, J. Xu, J. Yang, A new class of efficient and robust energy stable schemes for gradient flows, SIAM Rev. 61 (2019) 474–506.
[59] J.X. Yang, J. Kim, Energy dissipation-preserving time-dependent auxiliary variable method for the phase-field crystal and the Swift-Hohenberg models, Numer. Algorithms 89 (2022) 1865–1894.
[60] J. Shen, J. Xu, J. Yang, The scalar auxiliary variable (SAV) approach for gradient flows, J. Comput. Phys. 353 (2018) 407–416.
[61] J. Shen, J. Xu, Convergence and error analysis for the scalar auxiliary variable (SAV) schemes to gradient flows, SIAM J. Numer. Anal. 56 (2018) 2895–2912.
[62] F. Lin, X.-M. He, X. Wen, Fast, unconditionally energy stable large time stepping method for a new Allen-Cahn type square phase-field crystal model, Appl. Math. Lett. 92 (2019) 248–255.
[63] X. Yang, On a novel fully decoupled, second-order accurate energy stable numerical scheme for a binary fluid-surfactant phase-field model, SIAM J. Sci. Comput. 43 (2021) B479–B507.
[64] X. Yang, A novel fully-decoupled, second-order and energy stable numerical scheme of the conserved Allen-Cahn type flow-coupled binary surfactant model, Comput. Meth. Appl. Mech. Eng. 373 (2021) 113502.
[65] X. Yang, A novel fully-decoupled, second-order time-accurate, unconditionally energy stable scheme for a flow-coupled volume-conserved phase-field elastic bending energy model, J. Comput. Phys. 432 (2021c) 110015.
[66] X. Yang, X.M. He, A fully-discrete decoupled finite element method for the conserved Allen-Cahn type phase-field model of three-phase fluid flow system, Comput. Meth. Appl. Mech. Eng. 389 (2022) 114376.
[67] X. Yang, X.M. He, Numerical approximations of flow coupled binary phase field crystal system: fully discrete finite element scheme with second-order temporal accuracy and decoupling structure, J. Comput. Phys. 467 (2022) 111448.
[68] G. Zhang, X.-M. He, X. Yang, A fully decoupled linearized finite element method with second-order temporal accuracy and unconditional energy stability for incompressible MHD equations, J. Comput. Phys. 448 (2022) 110752.
[69] J.L. Guermond, P. Minev, J. Shen, An overview of projection methods for incompressible flows, Comput. Methods Appl. Mech. Eng. 195 (2006) 6011–6045.
[70] J.L. Guermond, J. Shen, On the error estimates for the rotational pressure-correction projection methods, Math. Comp. 73 (2004) 1719–1737.
[71] J. Shen, On error estimates of the projection methods for the Navier-Stokes equations: second-order schemes, Math. Comp. 65 (1996) 1039–1065.
[72] J. Li, X. Wang, M.A.A. Mahbub, H.B. Zheng, Z.X. Chen, Local and parallel efficient BDF2 and BDF3 rotational pressure-correction schemes for a coupled Stokes/Darcy system, J. Comput. Appl. Math. 412 (2022) 114326.

[73] B. Xie, Y.C. Huang, F. Xiao, A high-fidelity solver based on hybrid numerical methods on unstructured grids for incompressible multiphase flows, J. Comput. Phys. 463 (2022) 111299.
[74] J. Manzanero, G. Rubio, D.A. Kopriva, E. Ferrer, E. Valero, An entropy-stable discontinuous Galerkin approximation for the incompressible Navier-Stokes equations with variable density and artificial compressibility, J. Comput. Phys. 408 (2020) 109241.
[75] L. Lundgren, M. Nazarov, A high-order artificial compressibility method based on Taylor series time-stepping for variable density flow, J. Comp. Appl. Math. 421 (2023) 114846.
[76] Y. Qin, Y. Wang, Y.R. Hou, J. Li, An unconditionally stable artificial compression method for the time-dependent groundwater-surface water flows, Numer. Methods Partial Differ. Eqs. 39 (2023) 3705–3724.
[77] J.J. Yang, S.P. Mao, X.M. He, X.F. Yang, Y.N. He, A diffuse interface model and semi-implicit energy stable finite element method for two-phase magnetohydrodynamic flows, Comput. Methods Appl. Mech. Eng. 356 (2019) 435–464.
[78] J. Shen, X.F. Yang, A phase-field model and its numerical approximation for two-phase incompressible flows with different densities and viscosities, SIAM J. Sci. Comput. 32 (2010) 1159–1179.
[79] J.L. Guermond, L. Quartapelle, A projection FEM for variable density incompressible flows, J. Comput. Phys. 165 (2000) 167–188.
[80] C. Liu, J. Shen, A phase field model for the mixture of two incompressible fluids and its approximation by a Fourier-spectral method, Phys. D 179 (2003) 211–228.
[81] R.H. Nochetto, A.J. Salgado, S.W. Walker, A diffuse interface model for electrowetting with moving contact lines, Math. Models Methods Appl. Sci. 24 (2014) 67–111.
[82] V. Girault, P.A. Raviart, Finite element approximation of the Navier-Stokes equations: Theory and Algorithms, Springer-Verlag, Berlin, 1979.
[83] X.Y. Chen, R. Li, J. Li, The linear, decoupled and fully discrete finite element methods for simplfied two-phase ferrohydrodynamics model, Appl. Numer. Math. 210 (2025) 123–146.
[84] J. Shen, X.F. Yang, Energy stable schemes for Cahn-Hilliard phase-field model of two-phase incompressible flows, Chinese Ann. Math. Ser. B 31 (2010) 743–758.
[85] J. Shen, X.F. Yang, Decoupled energy stable schemes for phase field models of two phase complex fluids, SIAM J. Sci. Comput. 36 (2014) B122–B145.
[86] Y. Gao, D. Han, X.-M. He, U. Rüde, Unconditionally stable numerical methods for Cahn-Hilliard-Navier-Stokes-Darcy system with different densities and viscosities, J. Comput. Phys. 454 (2022) 110968.
[87] Y.L. Gao, X.M. He, T. Lin, Y.P. Lin, Fully decoupled energy-stable numerical schemes for two-phase coupled porous media and free flow with different densities and viscosities, ESAIM Math. Model. Numer. Anal. 57 (2023) 1323–1354.
[88] Y. Gao, X.-M. He, L. Mei, X. Yang, Decoupled, linear, and energy stable finite element method for the Cahn-Hilliard-Navier-Stokes-Darcy phase field model, SIAM J. Sci. Comput. 40 (2018) B110–B137.
[89] X.M. He, N. Jiang, C.X. Qiu, An artificial compressibility ensemble algorithm for a stochastic Stokes-Darcy model with random hydraulic conductivity and interface conditions, Int. J. Numer. Meth. Eng. 121 (2020) 712–739.
[90] N. Jiang, Y. Li, H.H. Yang, An artificial compressibility Crank-Nicolson leap-frog method for the Stokes-Darcy model and application in ensemble simulations, SIAM J. Numer. Anal. 59 (2021) 401–428.
[91] G. Bellettini, M. Paolini, C. Verdi, Γ-convergence of discrete approximations to interfaces with prescribed mean curvature, Atti Accad. Naz. Lincei Cl. Sci. Fis. Mat. Natur. Rend. Lincei Mat. Appl. 1 (1990) 317–328.
[92] A. Braides, N.K. Yip, A quantitative description of mesh dependence for the discretization of singularly perturbed nonconvex problems, SIAM J. Numer. Anal. 50 (2012) 1883–1898.
[93] C.M. Elliott, A.M. Stuart, The global dynamics of discrete semilinear parabolic equations, SIAM J. Numer. Anal. 30 (1993) 1622–1663.
[94] L. Chen, iFFM: an innovative finite element methods package in MATLAB, Preprint, University of Maryland (2008).
[95] M.R. Hassan, C. Wang, Lateral migration of a ferrofluid droplet in a plane Poiseuille flow under uniform magnetic fields, Phys. Rev. E. 102 (2020) 022611.
[96] Y. Chen, J. Shen, Efficient, adaptive energy stable schemes for the incompressible Cahn-Hilliard Navier-Stokes phase-field models, J. Comput. Phys. 308 (2016) 40–56.
[97] B.S. Hosseini, S. Turek, M. Möller, C. Palmes, Isogeometric analysis of the Navier-Stokes-Cahn-Hilliard equations with application to incompressible two-phase flows, J. Comput. Phys. 348 (2017) 171–194.
[98] J. Manzanero, G. Rubio, D.A. Kopriva, E. Ferrer, E. Valero, Entropy-stable discontinuous Galerkin approximation with summation-by-parts property for the incompressible Navier-Stokes/Cahn-Hilliard system, J. Comput. Phys. 408 (2020) 109363.
[99] J. Shen, X.F. Yang, Decoupled, energy stable schemes for phase-field models of two-phase incompressible flows, SIAM J. Num. Anal. 53 (2015) 279–296.
[100] C.H. Zhang, L.P. Wang, H. Liang, Z.L. Guo, Central-moment discrete unified gas-kinetic scheme for incompressible two-phase flows with large density ratio, J. Comput. Phys. 482 (2023) 112040.
[101] Y.D. Zeng, H. Liu, Q. Gao, A. Almgren, A.P.S. Bhalla, L. Shen, A consistent adaptive level set framework for incompressible two-phase flows with high density ratios and high Reynolds numbers, J. Comput. Phys. 478 (2023) 111971.
[102] M. Sussman, P. Smereka, S. Osher, A Level set approach for computing solutions to incompressible two-phase flow, J. Comput. Phys. 114 (1994) 146–159.
[103] K. Ueno, M. Higashitani, S. Kamiyama, Study on single bubbles rising in magnetic fluid for small Weber number, J. Magn. Magn. Mater. 149 (1995) 104–107.
[104] Y. Li, X.D. Niu, A. Khan, D.C. Li, H. Yamaguchi, A numerical investigation of dynamics of bubbly flow in a ferrofluid by a self-correcting procedure-based lattice Boltzmann flux solver, Phys. Fluids. 31 (2019) 082107.
[105] K. Ueno, T. Nishita, S. Kamiyama, Numerical simulation of deformed single bubbles rising in magnetic fluid, J. Magn. Magn. Mater. 201 (1999) 281–284.
[106] M.S. Korlie, A. Mukherjee, B.G. Nita, J.G. Stevens, A.D. Trubatch, P. Yecko, Modeling bubbles and droplets in magnetic fluids, J. Phys. Condens. Matter 20 (2008) 204143.
[107] A.S. Dizaji, M. Mohammadpourfard, H. Aminfar, A numerical simulation of the water vapor bubble rising in ferrofluid by volume of fluid model in the presence of a magnetic field, J. Magn. Magn. Mater. 449 (2018) 185–196.
[108] X. Li, Z.Q. Dong, Y.Y. Li, H. Yamaguchi, P. Yu, Magnetic field induced acceleration or deceleration of bubble rising inside ferrofluids: A fractional step lattice Boltzmann investigation, J. Magn. Magn. Mater. 591 (2024) 171750.
[109] C. Singh, A.K. Das, P.K. Das, Levitation of non-magnetizable droplet inside ferrofluid, J. Fluid Mech. 857 (2018) 398–448.
[110] R. Ahmed, M. llami, J. Bant, B. Beigzadeh, H. Marvi, A shapeshifting ferrofluidic robot, Soft Robot. 8 (2021) 687–698.
[111] X.J. Fan, M.M. Sun, L.N. Sun, H. Xie, Ferrofluid droplets as liquid microrobots with multiple deformabilities, Adv. Funct. Mater. 30 (2020) 2000138.
[112] D.Z. Hua, X.H. Liu, W.H. Li, G. Królczyk, R. Malekian, Z.X. Li, A novel ferrofluid rolling robot: Design, manufacturing, and experimental analysis, IEEE Trans. Instrum. Meas. 70 (2021) 1–10.
[113] H. Kitamori, S. Kudoh, J. Shintake, Robot locomotion by fluid-fluid interaction, Sci. Rep. 13 (2023) 21994.
[114] Y. Xiao, S. Zarghami, K. Wagner, P. Wagner, K.C. Gordon, L. Florea, D. Diamond, D.L. Officer, Moving droplets in 3D using light, Adv. Mater. 30 (2018) 1801821.
[115] J.-M. Roux, Y. Fouillet, J.-L. Achard, 3D droplet displacement in microfluidic systems by electrostatic actuation, Sens. Actuator A Phys. 134 (2007) 486–493.
[116] Y.M. Ji, C.Y. Gan, Y.G. Dai, X. Bai, Z.X. Zhu, L. Song, L.Y. Wang, H.W. Chen, J. Zhong, L. Feng, Deformable ferrofluid microrobot with omnidirectional self-adaptive mobility, J. Appl. Phys. 131 (2022) 064701.
[117] X.J. Fan, Y.F. Zhang, Z.G. Wu, H. Xie, L.N. Sun, T. Chen, Z. Yang, Combined three dimensional locomotion and deformation of functional ferrofluidic robots, Nanoscale 15 (2023) 19499–19513.

[118] Y.C. Zhang, L. Qin, J.Y. Wang, W. Xu, A liquid-solid mixed robot based on ferrofluid with high flexibility and high controllability, Appl. Phys. Lett. 121 (2022) 122402.
[119] J. Zhang, M.R. Hassan, B. Rallabandi, C. Wang, Migration of ferrofluid droplets in shear flow under a uniform magnetic field, Soft Matter 15 (2019) 2439–2446.
[120] D. Liang, P.C. Ma, C.Y. Zhu, T.T. Fu, Y.G. Ma, K. Wang, G.S. Luo, Manipulable formation of ferrofluid droplets in Y-Shaped flow-focusing microchannels, Ind. Eng. Chem. Res. 58 (2019) 19226–19238.
[121] P.F. Yuan, Q.X. Cheng, Y. Hu, Q. He, W.F. Huang, D.C. Li, Phase-field-based finite element model for two-phase ferrofluid flows, Phys. Fluids. 36 (2024) 022016.
[122] C. Gollwitzer, G. Matthies, R. Richter, I. Rehberg, L. Tobiska, The surface topography of a magnetic fluid: a quantitative comparison between experiment and numerical simulation, J. Fluid Mech. 571 (2007) 455–474.